Sensitivity of Tropical Cyclone Inner-Core Size and Intensity to the Radial Distribution of Surface Entropy Flux

Jing Xu and Yuqing Wang[1]

International Pacific Research Center and Department of Meteorology

University of Hawaii at Manoa, Honolulu, HI 96822

November 18, 2009 (submitted)

January 27, 2010 (revised)

Dateline

Revised for ***Journal of the Atmospheric Sciences***

[1] Corresponding author: Dr. Yuqing Wang, IPRC/SOEST, University of Hawaii at Manoa, 1680 East-West Road, Honolulu, HI 96822, Email: yuqing@hawaii.edu

Abstract

The surface energy (entropy) flux is critical to the development and maintenance of a tropical cyclone (TC). However, it is unclear how sensitive the inner-core size and intensity of a TC could be to the radial distribution of the surface entropy flux under the TC. Such a potential sensitivity is examined in this study using the multiply nested, fully compressible, nonhydrostatic TC model–TCM4. By artificially eliminating the surface entropy fluxes in different radial extent in different experiments, the effect of the surface entropy flux in the different radial range on the inner-core size and intensity of a simulated TC is evaluated. Consistent with recent findings from axisymmetric models, the entropy flux in the eye region of a TC is found to contribute little to the storm intensity but play a role in reducing the radius of maximum wind (RMW). Although surface entropy fluxes under the eyewall contribute greatly to the storm intensity, those outside the eyewall up to a radius of about 2-2.5 times the RMW are also important. Further outward, the surface entropy fluxes are found to be crucial to the growth of the storm inner-core size but could reduce the storm intensity. The surface entropy flux outside the inner core plays a critical role in maintaining high convective available potential energy (CAPE) outside the eyewall and thus active spiral rainbands. The latent heat release in these rainbands is responsible for the increase in the inner-core size of the simulated TC. A positive feedback is identified to explain changes in the RMW and the inner-core size of the simulated storms in different experiments. Implications of the results to both observations and numerical prediction of TC structure and intensity changes are briefly discussed.

1. Introduction

Tropical cyclones (TCs) intensify and maintain themselves against surface frictional dissipation by extracting energy from the underlying warm oceans. Therefore, energy exchange at the air-sea interface is the key to the intensity change of a TC (Malkus and Riehl 1960; Black and Holland 1995). The wind-induced surface heat exchange (WISHE), which describes a positive feedback between the increase in surface energy flux and the surface wind speed in the near core region of a TC, is viewed as the dominant process that controls the rapid intensification of a TC (Emanuel 1986; Rotunno and Emanuel 1987). On the other hand, Emanuel (1995, 1997) viewed the maximum potential intensity of a TC (E-MPI) as a state when the energy input from the ocean under the eyewall is locally balanced by the energy loss due to surface friction.

Recent studies with very high-resolution models show that the simulated TC maximum intensity expressed as the near-surface maximum wind speed can exceed the E-MPI by as much as 10-50% (Persing and Montgomery 2003, 2005; Cram et al. 2007; Yang et al. 2007; Bryan and Rotunno 2009; Wang and Xu 2010). Other studies show that the observed TC maximum intensity can be considerably stronger than the E-MPI (Montgomery et al. 2006; Bell and Montgomery 2008). Persing and Montgomery (2003) proposed that the near-surface high entropy air in the eye region could be a surplus energy source for the TC if the air is transported into the eyewall and thus, could considerably increase the TC intensity. This possibility, which is not included in the E-MPI theory, has been recently evaluated by Bryan and Rotunno (2009, hereafter BR09). In their axisymmetric TC model, BR09 set the surface entropy fluxes in the eye

region to zero to eliminate the local high-entropy anomaly near the surface in the eye. BR09 showed that this removal of high entropy anomaly in the eye only resulted in a reduction of about 4% in the maximum tangential wind speed, far too small to explain the higher maximum intensity in the simulation than the E-MPI. They found that only less than 3% of the total surface entropy input to the TC comes from the eye because of the small volume of the eye region. As a result, the total magnitude of entropy transport from the eye to the eyewall is negligible to the entropy budget and the intensity of the simulated TC.

The only possibility for the additional energy source for the TC should therefore be the energy input from outside of the eyewall. This possibility has recently been evaluated by Wang and Xu (2010, hereafter WX10) in a three-dimensional nonhydrostatic cloud-resolving TC model. WX10 found that the local balance assumption used in E-MPI does not hold in their numerically simulated TC and showed that the frictional dissipation rate is generally larger than the energy production rate under the eyewall. They demonstrated by a Lagrangian and a control volume equivalent potential temperature budget analyses that frictional dissipation under the eyewall is partly balanced by the inward transport of energy from outside of the eyewall. WX10 also showed in a sensitivity experiment that the storm maximum intensity can be reduced by 13.5% if the surface entropy fluxes outside 30-45 km away from the storm center were removed. In addition, WX10 found that the storm inner-core size in their sensitivity experiment is greatly reduced compared to the control experiment that includes the surface entropy fluxes outside the eyewall. This suggests that the storm inner-core size of the simulated storm depends substantially

on the surface entropy fluxes outside the eyewall.

Although WX10 have demonstrated the importance of the energy production outside the eyewall to the TC maximum intensity, the questions remain as to (1) within what radial extent outside the eyewall the energy production is critical to TC maximum intensity, (2) how far the surface entropy fluxes from the storm center are effective to affect the storm inner-core size and maximum intensity, and (3) what physical mechanisms are involved. These issues will be addressed in this study through a series of sensitivity numerical experiments and diagnostic analyses. The inner-core size of the TC herein is defined as the radius of the damaging wind (RDW, 25.7 m s^{-1}, Knaff et al. 2007) outside the eyewall while the maximum intensity is defined as the maximum azimuthal mean wind speed though the minimum sea level pressure is also examined.

The rest of the paper is organized as follows. Section 2 describes the numerical model and the design of numerical experiments. Section 3 discusses the possible effect of the near-surface high-entropy air in the eye region on the storm maximum intensity and the inner-core size in our three-dimensional model to validate the previous findings based on axisymmetric models. The sensitivity of the inner-core size and the maximum intensity of the simulated TC to the radial distribution of surface entropy flux outside the eyewall are analyzed in section 4. Links of our findings to previous studies and their implications are discussed in section 5. Main conclusions are drawn in the last section.

2. Model and experimental design

The model used in this study is the fully compressible, nonhydrostatic tropical cyclone model–TCM4 developed by Wang (2007). A full description of TCM4 can be found in Wang (2007), and its applications to the studies of the inner-core dynamics of TCs can be found in Wang (2008a and b, 2009) and WX10. The model settings are the same as those used in WX10.

The model uses the mass coordinate in the vertical with the lower boundary at a flat surface with the unperturbed surface pressure of 1010 hPa and with its top at about 38 km. The model domain is quadruply nested with two-way interactive nesting and with the inner meshes automatically moving to follow the model storm (Wang 2001, 2002c). The model has 26 vertical levels with relatively high resolution both in the lower troposphere and near the tropopause. The horizontal grid intervals of 67.5, 22.5, 7.5, and 2.5 km have domain sizes of 251×151, 109×109, 127×127, and 163×163 grid points for the four meshes, respectively.

The model physics include an E-ε turbulence closure scheme for subgrid scale vertical turbulent mixing (Langland and Liou 1996), a modified Monin-Obukhov scheme for the surface flux calculations (Fairall et al. 2003), an explicit treatment of mixed-phase cloud microphysics (Wang 2001), a nonlinear fourth-order horizontal diffusion for all prognostic variables except for that related to the mass conservation equation, a simple Newtonian cooling term to mimic the radiative cooling (Rotunno and Emanuel 1987), and the dissipative heating due to molecular friction related to the turbulent kinetic energy dissipation rate (ε) from the E-ε turbulent closure scheme. As in Wang (2007, 2008a and b, 2009), the same model physics are used in all meshes. Since no large-scale environmental flow is included in this study, convection occurs mainly in both the inner-core region and the spiral rainbands within about 200 km from the TC center and is covered by the finest innermost domain. Therefore, cumulus parameterization is not considered in any mesh in this study.

The experimental design follows Wang (2008a and b, 2009). The model was initialized with an axisymmetric cyclonic vortex on an *f*–plane of 18^{o}N in a quiescent environment over the ocean with a constant SST of 29^{o}C. The initial thermodynamic structure of the unperturbed model atmosphere is defined as the western Pacific clear-sky environment given by Gray et al. (1975). The initial cyclonic vortex has a maximum tangential wind speed at the surface of 20 m s^{-1} at a radius of 80 km that decreases sinusoidally with pressure to vanish at 100 hPa. The mass and thermodynamic fields are obtained by solving the nonlinear balance equation as described in Wang (2001). The initial model TC that was used in all experiments described below was first spun up for 48 h with all default model settings. After this spin-up period, the model TC developed a structure similar to real TCs (Fig. 1).

The storm has its maximum tangential wind of over 50 m s^{-1} in the lowest 1 km layer at a radius of about 20 km (Fig. 1a), a shallow inflow layer in the boundary layer, and a relatively deep outflow layer in the upper troposphere (Fig. 1b). The eyewall ascent tilts radially outward with height, especially above the altitude of 5 km (Fig. 1c). The storm has a warm-core structure through the depth of the troposphere with the maximum temperature anomaly over 9^{o}C in the eye region in the upper troposphere (Fig. 1d). There are some negative temperature anomalies under and outside the eyewall mainly due to the evaporation of rain water. The storm shows an off-centered potential vorticity (PV) maximum just inside the RMW through the depth of the troposphere (Fig. 1e). Equivalent potential temperature (θ_e) is high in the eye and eyewall with local maxima near the surface in the eye and in the upper troposphere (Fig. 1f). Relatively high θ_e also appears in the inflow boundary layer and increases gradually toward the eyewall near the surface, an indication of the inflow boundary layer air acquiring energy from the underlying ocean as the air spirals cyclonically inward toward the eyewall.

Nine numerical experiments were performed (Table 1). In the control experiment (CTRL), the model was integrated with all default model settings as used in the spin-up period. In the second and third experiments (IE1 and IE2), the surface entropy (sensible and latent heat) fluxes were artificially set to zero within the RWM (r_m) and $0.8r_m$, respectively. Note that the TC center is defined in this study as the center of axisymmetric circulation along which the azimuthal mean wind at the lowest model level (about 35 m) reaches the maximum at a given time. Different from BR09 in an axisymmetric model, r_m in this study represents the mean radius of the eyewall, which is characterized by the maximum tangential winds and strong upward motion. The actual radius of the eyewall in each quadrant could deviate from the mean r_m due to the elliptical and polygonal eyewall structures in the simulation (Wang 2002a, b). Since r_m is time dependent, the eye volume is expected to vary with time in our simulation. Experiments IE1 and IE2 were designed to examine the possible contribution of the near-surface high-entropy air in the eye to the model TC intensity as done in BR09 but in a three-dimensional model and also the effect on the model TC eyewall size.

In the remaining experiments, the surface entropy fluxes were eliminated at different radii outside the eyewall. Specifically, surface entropy flux was modified with a weighting function which is unit within a radius R_1, decreases linearly outward from R_1 to zero at a radius R_2, and remains zero further outward. In experiments OE30, OE45, OE60, OE75, OE90, and OE120, (R_1, R_2) are set to be (30km, 45km), (45km, 60km), (60km, 75km), (75km, 90km), (90km, 120km), and (120km, 150km), respectively. Experiments OE30-OE120 (Table 1, hereafter also OEs in brief) were designed to understand how significant the surface entropy fluxes outside the eyewall would be to the simulated TC inner-core size and intensity.

3. Sensitivity to surface entropy flux in the eye

Since the effect of surface entropy fluxes in the eye on the TC maximum intensity has been comprehensively studied in an axisymmetric model by BR09, we will only briefly discuss the results from our three-dimensional simulations. Since the eyewall of the simulated storm can be asymmetric from time to time (Wang 2007), we only use the azimuthal mean RMW as a proxy of the location of the overall eyewall. Simple checks indicate that the RMW varies in different directions with maximum variances less than 20% of the azimuthal mean RMW at the lowest model level in the simulated storm because the model was run on an *f*-plane in a quiescent environment. As a result, in our sensitivity experiment IE1, the cutoff of surface entropy flux within the azimuthal mean RMW also eliminated part of the surface entropy fluxes in the inner-edge of the eyewall, while in experiment IE2, the removal of surface entropy fluxes within 0.8RMW was only occurred in the eye region and therefore, had little effect on surface entropy fluxes under the eyewall.

Figure 2 shows the evolution of the maximum azimuthal mean tangential wind at the lowest model level and the minimum sea level pressure (MSLP) in experiments CTRL, IE1 and IE2. The lifetime maximum intensity of the model storm in IE1 (IE2) is weaker than that in CTRL, namely 63 m s^{-1} (67 m s^{-1}) versus 70 m s^{-1} in the maximum azimuthal mean wind speed (Table 1) and 928 hPa (915 hPa) versus 906 hPa in the MSLP, or about 10% (4.3%) weaker in the maximum azimuthal mean wind speed and about 22 hPa (9 hPa) higher in the MSLP. Therefore, the surface entropy fluxes in the eye contribute positively to the storm intensity, but this is not enough to explain the higher maximum intensity of the simulated storm than the E-MPI, which is about 41.5 m s^{-1} for the initial sounding used in our simulation (see WX10 for details). As we can see, even though part of the surface entropy fluxes under the eyewall were

removed in IE1, the storm is only about 10% weaker in the maximum azimuthal mean wind speed than the storm in CTRL because of the small volume of the eye. This result is consistent with the finding of BR09.

In the control experiment, the near surface air in the eye has the highest θ_e in both developing and mature stages (Figs. 3a and 3d). θ_e in the eyewall is more than 15 K lower than that in the eye in CTRL. With the removal of the surface entropy fluxes in the eye region in both IE1 and IE2, the near surface θ_e in the eye is greatly reduced compared to that in CTRL. As a result, throughout the simulation in IE1 and in the developing stage in IE2, the near surface θ_e is the highest slightly inside the RMW (Figs. 3 and 4). However, in the mature stage, the near surface θ_e is again high and uniform in the eye region in IE2 (Figs. 3f and 4c) but the magnitude is still more than 10 K lower than that in CTRL (Figs. 3a, 3d, and 4a). Since such near-surface high θ_e in the eye in CTRL only results in about 4.3% stronger maximum low-level azimuthal mean wind of the storm than that in IE2, we can conclude that the near-surface high energy air in the eye could not be a major energy source for the storm. The insignificant contribution by the near surface high-energy in the eye is also reflected in the area-averaged energy production rate in CTRL as shown in WX10. The net energy production near the storm center is indeed negative due to radiative cooling in the eye.

In addition to a slightly weakening storm due to the removal of surface entropy fluxes in the eye region, the RMW of the simulated storm was increased by 10% and 20%, respectively, in IE2 and IE1 (Fig. 5 and Table 1). The removal of surface fluxes in the eye region had little effect on the vortex scale circulation outside the eyewall while reduced the circulation in the eye (Figs. 5a and b). Further, θ_e in the eye was up to 12 K lower than that in the eyewall in IE1, in contrast to those in CTRL and IE2 where θ_e is higher in the eye than in the eyewall (Fig. 5c). However,

differences in θ_e averaged under the eyewall were relatively small. As a result of the slight increase in the RMW and the reduction of circulation in the eye region due to the removal of surface entropy fluxes in the eye region, potential vorticity (PV) in the eye and eyewall was reduced in both IE1 and IE2 compared to that in CTRL (Fig. 5d). Therefore, from the energetic point of view, though it is a distinct feature of a TC, the eye can be considered a "nearly" passive part of the storm and contributes little to the overall storm intensity (see also WX10).

4. Sensitivity to surface entropy flux outside the eyewall

a. Storm intensity

WX10 already demonstrated that the energy production outside the eyewall plays an important role in the energy balance in the eyewall and thus contributes to the storm intensity. Here, based on a series of sensitivity experiments, we examine within what radial extent outside the eyewall the energy production is critical to TC maximum intensity and how far the surface entropy fluxes from the storm center could effectively affect the storm inner-core size and maximum intensity. Different from BR09, who performed sensitivity experiments by removing surface entropy fluxes within a given radius, we eliminate surface entropy fluxes outside the radius of 30, 45, 60, 75, 90, and 120 km, respectively, in experiments OE30, OE45, OE60, OE75, OE90, and OE120. The extreme case of OE30 was the same as that discussed in WX10. It was designed to examine the effect of surface entropy fluxes immediately outside the eyewall since the mean eyewall updrafts are within a radius of about 30 km in the lower troposphere in CTRL (Fig. 1). The experiment OE120 was conducted to understand whether the energy production far away from the inner-core region plays an important role in affecting the inner-core size and intensity of the simulated storm.

Figure 6 compares the evolution of the maximum azimuthal mean tangential wind at the lowest model level and the MSLP in all experiments OEs with those in CTRL. Removal of surface entropy fluxes immediately outside the eyewall in OE30 results in a large reduction in the storm intensification rate after an initial adjustment of several hours and the weakest storm among these OEs experiments. Extending the cutoff radius to 45 km, the storm intensified roughly at the same rate as in CTRL in the first 72 h of simulation. This was followed by a steady weakening. However, the storms in OE60, OE75, OE90, and OE120 intensified with slightly higher intensification rates than that in CTRL in the first 72 h of simulation, indicating that surface entropy fluxes outside a radius of about 60 km may suppress the TC intensification in the early development stage of the TC in the simulation. Similar to the case for OE30, a dramatic transition from intensifying to weakening occurred after about 72-h simulation in other OEs experiments except in OE120 which showed a quasi-steady evolution of the storm intensity. The storm in OE90 had an intensity similar to that in OE120 while it was slightly stronger than the storm in CTRL in terms of the maximum low-level azimuthal mean wind speeds (Fig. 6a).

A similar transition from intensifying to weakening in the maximum low-level azimuthal mean wind also occurred in CTRL, but after about 120-h simulation, a situation which was related to the formation of an annular hurricane structure (see Wang 2008b) as identified by Knaff et al. (2003) from observations. Accompanying the decrease in the maximum low-level azimuthal mean wind was a considerable increase in the MSLP in OE30, OE45, OE60 and OE75. This, however, did not happen to the cases in CTRL, OE90, and OE120. The storms in both OE90 and OE120 did not experience any significant weakening after they reached their maximum intensity after 96-h simulation. The storms in both OE90 and OE120 showed an intensity evolution similar to but were stronger than the storm in CTRL throughout the

simulation. The lifetime maximum azimuthal mean low-level wind speed in OE90 was similar to that in CTRL, while that in OE120 was about 5-6% higher than that in CTRL. Note that the MSLP in both OE90 and OE120 was similar to that in CTRL. Therefore, surface entropy fluxes outside a radius of about 90 km could reduce the maximum TC intensity. This is mainly due to the fact that surface entropy fluxes at large radii favor the active outer spiral rainbands that generally form outside of the rapid filamentation zone (Rozoff et al. 2006; Wang 2008a) and reduce the TC intensity as recently studied by Wang (2009).

b. Storm inner-core size

We define the storm inner-core size in this study roughly the RMW and the radius of the azimuthal mean damaging wind (25.7 m s^{-1}) at the lowest model level since both the RMW and the radius of damaging wind (RDW) give good indications of winds or total kinetic energy in the boundary layer within a radius of about 150 km in our simulations. Although the RMW of the simulated storms in IE1 and IE2 was slightly increased due to the removal of surface entropy flux in the eye region compared to that in CTRL (Fig. 5), removal of surface entropy fluxes outside the eyewall resulted in a persistent decrease in both the RMW and the inner-core size of the simulated storms after some initial adjustments. As we can see from the azimuthal mean tangential wind at the lowest model level and vertical motion at a height of 5 km in Fig. 7, the inner-core size of the storm in CTRL increased gradually with time, that is, both its RMW and the low-level strong winds expanded outward (Fig. 7a). A similar increase in the inner-core size occurred in experiments with surface entropy fluxes removed outside a radius larger than 75 km in the early hours of simulation. This, however, did not occur in OE30, OE45, and OE60, in which the inner-core size of the storms decreased almost linearly with time (Fig. 7). The decrease in the inner-core size is inversely proportional to the radius outside which surface entropy fluxes

were removed, that is, the smaller the radius outside which the surface entropy fluxes were removed, the smaller the inner-core size of the storm. Therefore, in addition to the intensity, surface entropy fluxes outside the eyewall are very important to the inner-core size of the simulated storm.

Figure 8 shows examples of plan views of the surface rain rate in given experiments after 48 h and 144 h of simulations. By 48 h of simulation (Fig. 8a), although storms in all OEs were intensifying, the eyewall size decreased considerably as inferred from the heavy precipitation (Fig. 8a), particularly in experiments with the surface entropy fluxes removed outside a small radius, such as in OE30 and OE45. In the late stage, storms in OE30, OE45, OE60, and OE75 became very small with their RMW of about 7.5 km (Fig. 8b). This is probably the smallest eye and eyewall that our model resolution can resolve since the RMW is only 3 times the model horizontal grid spacing. Nevertheless, the model storm still possesses the characteristics of a TC, resembling the so-called midget TC in the western North Pacific (Brand 1972; Merrill 1984; Harr et al. 1996). The inner-core size of the storms in OE90 and OE120 is smaller than that in CTRL but is considerably larger than those in other experiments in the late stage. Another distinct feature of the storms in these sensitivity experiments is the absence of active outer spiral rainbands compared to the storm in CTRL (Fig. 8b).

The evolution of the overall inner-core size of the simulated storms is shown in Fig. 9 in terms of the RDW, the area-integrated azimuthal mean kinetic energy at the lowest model level, and the area-integrated surface entropy flux within 150 km radius. Consistent with the low-level azimuthal mean tangential wind shown in Fig. 7, both the RDM and the area-integrated azimuthal mean kinetic energy increased with time in CTRL, while both increased in the first 48-h simulation followed by a decrease in OE120 and decreased throughout the simulation in all

other OEs (Figs. 9a and 9b). The storm in CTRL is quite energetic with its area-integrated kinetic energy about 4 to 8 times of those in OEs. This is consistent with the energy input from the ocean as shown in the area-integrated surface entropy flux in Fig. 9c. Therefore, the storm inner-core intensity (as measured here by the area-integrated kinetic energy within a radius of 150 km) is not only determined by the energy production under the eyewall but is contributed considerably by the energy production outside the eyewall in a similar way to the storm maximum intensity as recently discussed in WX10.

Figure 10 compares some storm properties at the lowest model level after 144 h of simulation in CTRL and all OEs. The RMW and both the tangential and radial winds outside the RMW are considerably reduced as a result of the removal of surface entropy fluxes outside the eyewall (Figs. 10a and 10b). The reduction is directly proportional to the radius outside which the surface entropy fluxes were eliminated. θ_e is high in the eye region in all experiments and decreases rapidly outward across the RMW (Fig. 10c). θ_e at the lowest model level is greatly reduced at all radii in all OEs as a result of the removal of surface entropy fluxes outside some outer radius compared to that in CTRL. For example, θ_e in OE30, OE45, OE60, OE75, and OE90 is over 10 K lower than that in CTRL at all radii. Even though the storm in OE120 is stronger than that in CTRL, the low-level θ_e near the storm center is still more than 5 K lower than that in CTRL. This is consistent with the relatively higher MSLP in all OEs than that in CTRL after 192 h of simulation.

Storms in CTRL and OE120 showed off-center PV maximum just inside the RMW while storms with small inner-core size in other experiments exhibit a monotonic radial distribution with the maximum PV at the storm center (Fig. 10d). Since the radial monotonic (hollow) PV distribution implies a barotropically stable (unstable) eyewall structure (Schubert et al 1999),

both CTRL and OE120 are expected to favor the development of asymmetries in the eyewall. This is indeed the case as we can see from Fig. 11, which shows the radius-time cross-section of the azimuthal mean PV and azimuthal mean eddy kinetic energy (EKE)[2] averaged in the model lowest 3-km layer in given experiments. The asymmetries in the eyewall were relatively strong throughout the simulation in CTRL and OE120 (Figs. 11a and 11f) while those in other experiments weakened with time. This is consistent with the barotropic model results of Schubert et al. (1999), who showed that asymmetries could develop more quickly in storms having a hollow PV structure with larger eyewalls.

c. Dynamical mechanisms

Wang (2009) demonstrated that diabatic heating in active spiral rainbands plays a critical role in TC structure and intensity changes. Since surface entropy fluxes can affect the activity of spiral rainbands and thus diabatic heating outside the eyewall, we first examine how spiral rainbands respond to the modification of surface entropy fluxes in different experiments. Figure 12 shows the radial-time cross-section of the azimuthal mean surface rain rate and the azimuthal mean convective available potential energy (CAPE), which was calculated for a parcel lifted from the lowest model level in the given experiments. In CTRL, rainfall occurred not only in the eyewall but extended radially outward due to the existence of active spiral rainbands (Fig. 8). The large surface entropy fluxes outside the eyewall were responsible for the high CAPE and thus the active spiral rainbands in CTRL (Fig. 12a). The immediate responses to the removal of

[2] EKE is defined as $\frac{1}{2}(u'^2+v'^2)$, where u' and v' are asymmetric radial and tangential wind speeds, respectively.

surface entropy fluxes outside the eyewall in all OEs were the reduced CAPE and the suppressed activity of spiral rainbands in the simulated storms. Note that although rainfall was more concentrated in the eyewall in OE120 than in CTRL, considerable rainfall still occurred between the eyewall and the radius of 80 km due to active inner spiral rainbands (Figs. 8 and 12f) that are closely related to the convectively coupled vortex Rossby waves (Wang 2002a,b, 2008a), similar to the case in CTRL (Fig. 12a). In contrast, little rainfall occurred outside the radius of 40 km in OE30, OE45, OE60 and OE75 except in the first 72-h simulation. Different radial distribution of rainfall implies different radial distribution in diabatic heating outside the eyewall. This is the key to understanding the various inner-core sizes in different experiments.

As shown by Wang (2009), diabatic heating in active spiral rainbands could lower the surface pressure outside the RMW and reduce the pressure gradient across the RMW and thus, weaken the storm but increase the inner-core size of a TC. This can explain why the inner-core size of storms in all OEs was smaller than that in CTRL since spiral rainbands were greatly suppressed in all OEs compared to those in CTRL (Fig. 8). This can also explain why storms in OE90 and OE120 were stronger than that in CTRL in terms of the maximum azimuthal mean low-level wind speed throughout the simulation and why those in OE60 and OE75 were stronger during the early stage of the simulation (Fig. 6). However, it cannot explain why the storms in OE60 and OE75 were weaker during the later stage of the simulation. The weakening of storms in OE30, OE45, OE60, and OE75 seemed to be related to the decrease in storm inner-core size (Figs. 7 and 9). A major consequence of the inner-core size decrease was a more rapid decay of winds with radius outside the RMW (Figs. 7 and 10). This would lead to the reduced area coverage of high winds and reduced surface entropy fluxes in the inner-core region, especially for those in OE30, OE45, OE60, and OE75 since the surface entropy fluxes were eliminated

already outside a given radius (Figs. 7 and 9c). As the energy production due to surface entropy fluxes outside the eyewall plays an important role in the maximum TC intensity as discussed in WX10, the reduction of surface entropy fluxes immediately outside the eyewall would have an immediate effect on the storm intensity, such as the case in OE30. However, the reduction of energy production outside the eyewall in OE45, OE60, and OE75 had a delayed effect on the storm intensity. This effect was enhanced by the decrease in the storm inner-core size and the rapid decaying of winds with radius outside the eyewall in all OEs (Fig. 10a). Therefore, there exists a positive feedback between the reduced winds and surface entropy fluxes outside the eyewall, and the reduced inner-core size and intensity of the storm (Figs. 9 and 10).

We can see from Fig. 13 that as a result of the suppressed spiral rainbands in OEs due to the removal of surface entropy fluxes outside the eyewall, the low-level pressure near and outside the RMW was higher than that in CTRL (Fig. 13a). This increased the radial pressure gradient across the RMW in all OEs relative to that in CTRL (Fig. 13c)[3]. To understand how the storm inner-core size responds to changes in the radial pressure gradient associated with diabatic heating in spiral rainbands, we performed a momentum budget analysis below. The budget equations for the azimuthal mean radial and tangential winds can be approximated by

$$\frac{d\overline{u}}{dt} = -\frac{1}{\overline{\rho}}\frac{\partial \overline{p}}{\partial r} + \frac{\overline{V}^2}{r} + f\overline{V} + \overline{F}_u + \overline{D}_u, \tag{1}$$

$$\frac{\partial \overline{V}}{\partial t} = -\overline{u}\,\overline{\varsigma}_a - \overline{w}\frac{\partial \overline{V}}{\partial z} + \overline{F}_V - \overline{u'\varsigma'} - \overline{w'\frac{\partial V'}{\partial z}} + \overline{D}_V, \tag{2}$$

where r is radius, z is height, $\overline{u}, \overline{V}$, and $\overline{w}$ are azimuthal mean radial and tangential winds and vertical motion, $\overline{\varsigma}_a$ is the vertical absolute vorticity of the azimuthal mean flow, $\overline{\rho}$ and $\overline{p}$ are

[3] Note that Fig. 13 (and also Fig. 14) only shows the results for experiments OE60, OE120, and CTRL because results in all other experiments are quite similar to those in OE60 and thus are not shown.

air density and pressure, f is the Coriolis parameter, u', w', V', and ς' are deviations of radial, vertical, tangential winds, and vertical relative vorticity from their corresponding azimuthal mean values, $\overline{F}_u, \overline{F}_V, \overline{D}_u$, and $\overline{D}_V$ are parameterized subgrid scale vertical diffusion, including surface friction, of radial and tangential winds, and the horizontal diffusion of radial and tangential winds, respectively. Terms on the right hand side in (1) are radial pressure gradient force, centrifugal force, Coriolis force, and vertical and horizontal diffusion of radial wind, respectively. Terms on the right hand side in (2) are contributions of radial advection, vertical advection, vertical diffusion (including surface friction), eddy radial and vertical advections, and horizontal diffusion to the local tendency of tangential wind, respectively. Our calculations showed that the eddy transport and horizontal diffusion were quite small and negligible in the simulated storm (not shown). Note that the acceleration of radial wind in Eq. (1) reflects the gradient wind imbalance. This imbalance mainly results from the change in pressure gradient force associated with the hydrostatic adjustment to diabatic heating either in the eyewall or in the spiral rainbands or both as elaborated in Wang (2009).

The momentum budget is evaluated at the lowest model level for two time periods: time means between 24 and 72 h during the developing stage and between 120 and 168 h during the mature stage of the simulated storms (Fig. 6). In the first time period, storms were intensifying except for that in OE30 (Fig. 6). Storms in all OEs experienced an eyewall contraction (Fig. 7), mainly due to the increased radial pressure gradient force (Fig. 13c) and the inward penetration of the accelerating boundary layer inflow across the RMW (Figs. 10b and 14a). The inward penetration of low-level inflow across the RMW (Fig. 10b) increased the tangential wind speed inside the RMW through the azimuthal mean radial advection term ($-\overline{u}\overline{\varsigma}_a$, Fig. 14c) because of

the elevated absolute vorticity inside the RMW (Fig. 14e). This led to the contraction of the RMW (Fig. 7) and intensification of the storms in all OEs expect for that in OE30. Both in turn increased the absolute vorticity inside the RMW (Fig. 14e), which further enhanced the increase in tangential winds inside the RMW through the radial advection (Fig. 14c) and the contraction of the RMW. This is a positive feedback controlling the contraction of the RMW. The contraction resulted in a large centrifugal force, a deceleration of the boundary layer inflow, and induction of a supergradient wind, preventing further contraction of the RMW. The radial advection ($-\overline{u}\overline{\zeta}_a$) also caused a considerable increase in tangential winds outside the RMW in CTRL (Fig. 14c) due to the relatively large inflow outside the eyewall (Fig. 10b) and the relatively large absolute vorticity outside the RMW (Fig. 14e). This is a major mechanism for the outward expansion of tangential wind fields and the increase in the inner-core size of the storm in CTRL (Figs. 7 and 8). This mechanism in all OEs was not as effective as that in CTRL (Fig. 14c) because of the weaker boundary layer inflow and smaller absolute vorticity outside the eyewall in the former (Fig. 10b and 14e). As a result, instead of outward expansion, an inward contraction of the tangential wind fields occurred in all OEs except in OE120.

In the second time period, the storm in CTRL became much larger than those in OEs (Figs. 7 and 8) and showed active spiral rainbands, while rainbands were greatly suppressed in all OEs except in OE120 which exhibited active inner spiral rainbands (Fig. 8b). As a result, the surface pressure outside the eyewall did not change much in OEs but lowered considerably in CTRL due to the increase in the inner-core size (Fig. 13b) and diabatic heating in active spiral rainbands (Wang 2009). The RMW in OEs were quite small and showed little inward contraction due to high centrifugal force, which was largely balanced by the large pressure gradient force and deceleration of radial wind (Figs. 13d and 14b). The radial advection of angular momentum

still contributed considerably to the positive tendency of tangential wind outside the eyewall in CTRL (Fig. 14d). This gives rise to an overall outward expansion of tangential wind fields and the inner-core size with time in CTRL (Figs. 9 and 11a) although this tendency was greatly balanced by surface friction (not shown). However, there was no significant contribution by radial advection to the tangential wind tendency outside a radius of 30 km in all OEs during this period (Fig. 14d), which was consistent with the quasi-steady small inner-core size of the simulated storms in those experiments (Fig. 11).

The above momentum budget results demonstrate that the boundary layer inflow and its induced acceleration of tangential winds outside the eyewall are critical to the increase in the inner-core size of the simulated storm in CTRL. In turn, the boundary layer inflow, in particular that outside the eyewall, was dominantly controlled by diabatic heating in spiral rainbands. Therefore, a positive feedback exists between active spiral rainbands and the increase in the inner-core size of the storm in CTRL. This positive feedback can also explain the decrease in the inner-core size of storms in all OEs. Removal of surface entropy fluxes outside a certain radius in OEs reduced the CAPE outside the eyewall and suppressed spiral rainbands, which, in turn, reduced diabatic heating outside the eyewall. This greatly reduced the boundary layer inflow outside the eyewall, limiting the outward expansion of tangential wind fields. This latter then reduced surface entropy fluxes even within the radius outside which surface entropy fluxes were removed, such as in the case of OE120 (Fig. 9c), further reducing the CAPE outside the eyewall and suppressing spiral rainbands. In the intensifying stage, this positive feedback explains the contraction of both the RMW and wind fields in all OEs (Fig. 6). In the mature stage, this positive feedback helped maintain the small inner-core size in all OEs while contributed to the outward expansion of tangential wind fields in CTRL since the storm in CTRL developed active

spiral rainbands.

5. Discussion

Weatherfort and Gray (1988a) defined the "inner-core" of a TC as the region from the storm center to about 1^o latitude radius, while the "outer core" as the region between 1^o and 2.5^o latitude radii. They showed that changes in the inner-core strength often occur independently from those in the outer-core strength. While the inner-core strength is closely related to the storm intensity, the outer-core strength seems to be affected greatly by the synoptic environmental conditions (Merrill 1984; Holland and Merrill 1984; Weatherfort and Gray 1988b; Cocks and Gray 2002). In this study, we defined the inner-core to extend from the storm center to the RDW outside the eyewall. Therefore, the inner-core size varies with time for a given storm by our definition. Previous studies have showed that the RDW varies from less than 40 km to over 120 km for hurricane-intense storms (Kimball and Mulekar 2004; Moyer et al. 2007). However, there have been few discussions on what controls the inner-core size of a TC. Maclay et al. (2008) examined the evolution of TC inner-core kinetic energy based on wind fields from aircraft reconnaissance flight level data. They found two processes that may lead to the growth of TC inner-core size: (1) secondary eyewall formation and eyewall replacement cycles and (2) external forcing from the synoptic environment, such as the vertical shear. These findings can be physically explained by the mechanisms that we have detailed in the last section. The formation of secondary eyewall is accompanied by strong diabatic heating in the outer eyewall outside the primary eyewall (Willoughby et al. 1982). This would lead to increase in tangential winds outside the primary eyewall, thus increasing the inner-core size of the TC. Interaction between a TC and vertical shear can result in main spiral rainbands downshear (Willoughby et al. 1984).

Convective heating in the rainbands may thus lead to increase in the inner-core size of the TC in vertical shear.

The inner-core size change in response to diabatic heating in spiral rainbands can also be understood from PV thinking (May and Holland 1999; Hill and Lackmann 2009). May and Holland (1999) suggested that cyclonic PV anomalies generated in spiral rainbands could be a significant inner-core PV source in a TC, affecting the TC structure and intensity. This possible mechanism has been recently studied by Hill and Lackmann (2009) who investigated how environmental humidity affects the TC size in idealized simulations. They showed that a relatively dry environment produced less rainfall outside the TC core due to suppressed spiral rainbands, a narrower eyewall, and less radial outward expansion of wind fields, than a moist environment did. They demonstrated that diabatic PV generation in spiral rainbands and subsequent radial transport are critical to the outward expansion of wind fields and thus the increase in the inner-core size of the simulated storm in a relatively moist environment. In our simulations, spiral rainbands of the simulated storms were greatly suppressed in OEs with surface entropy fluxes removed beyond a given radius outside the eyewall. Therefore, the smaller inner-core size of the simulated TCs in OEs as compared to that in CTRL is due to the lack of active spiral rainbands, which is consistent with the PV thinking (May and Holland 1999; Hill and Lackmann 2009).

Hill and Lackmann (2009) also pointed out that vortex Rossby waves in the eyewall could lead to expansion of the eye and weakening of inner-core PV gradient in their relatively moist environment experiment. We have shown in Fig. 11 that storms with a relatively larger eyewall in CTRL and OE120 exhibit stronger asymmetries across the eyewall, indicating the existence of vortex Rossby waves in the eyewall and the activity of inner spiral rainbands (Wang

2001, 2002a,b). These waves mix PV both inward and outward across the eyewall, reducing the PV gradient across the eyewall and increasing the inner-core size in CTRL as shown in Fig. 10d, consistent with the results of Hill and Lackmann (2009). This mechanism was greatly suppressed due to the lack of active spiral rainbands and thus less lateral PV mixing across the eyewall in all other experiments (Figs. 10d and 11). Therefore, there seems another positive feedback in the control of the eyewall size in a TC. Inward transport of cyclonic PV produced in active spiral rainbands would increase PV in the inner core of the storm which would increase the size of the eyewall and thus the RMW. This would result in the development of an elevated PV ring just inside the enlarged eyewall, destabilizing the eyewall and leading to the development of asymmetries in the eyewall (Schubert et al. 1999), which will mix the eyewall PV both inward and outward, further increasing the inner-core size of the storm.

In a recent modeling study, Smith et al. (2009) identified two mechanisms responsible for the spin-up of the mean tangential circulation, namely, the convergence of absolute angular momentum above the boundary layer for the spin-up of the outer circulation, which increases the TC size, and that within the boundary layer for the spin-up of the inner-core circulation. They indicated that the first mechanism is related to deep, inner-core convection in the presence of enhanced surface moisture fluxes and can be interpreted in terms of balanced dynamics, while the second mechanism is responsible for the spin-up of the inner core and is related to the overshooting of the frictional boundary layer inflow. Both mechanisms were discussed earlier by Ooyama (1969, 1982) and they work well in our numerical experiments discussed in the last section. In our numerical experiments, the boundary layer inflow induced by eyewall heating and enhanced by surface friction can penetrate into the RMW and contributes to the contraction of the RMW. Heating outside the eyewall contributes significantly to the spin-up of tangential

winds outside the RMW and thus the outward expansion of wind fields and the increase in the inner-core size of the storms. Therefore, different from Smith et al. (2009), this study emphasizes the importance of diabatic heating in spiral rainbands to the inner-core size of a TC.

Although our numerical experiments were designed to examine the sensitivity of the inner-core size and intensity of TCs to the radial distribution of surface entropy flux, the results have implications to both TC observations and the initialization of TC vortex in numerical weather prediction models. The inner core of a TC consists of the most severe weather. Its size determines the extent of potential damage that may results from an approaching TC. However, direct measurements in the inner core of TCs over the open ocean are very limited. Our results suggest that storms that are rich in active spiral rainbands potentially have large inner-core sizes. Therefore, high-resolution satellite imageries may be practically useful for estimating the inner-core size of TCs (Demuth et al. 2006; Kossin et al. 2007). Results from this study also suggest that accurate representation of the initial storm structure, such as the radial distribution of absolute vorticity, is important to the skillful prediction of the evolution of the storm inner-core size and intensity in a dynamical model. Initialization of humidity and even the spiral rainbands could be important too. In addition, the boundary layer physics and the details in cloud microphysics may affect the predicted activity of spiral rainbands and thus, the storm inner-core size and intensity in a dynamical model (e.g., Wang 2002c).

6. Conclusions

The sensitivity of the inner-core size and intensity of a TC to the radial distribution of surface entropy flux has been studied using a three-dimensional cloud-resolving TC model by artificially eliminating surface entropy fluxes in different radial extents. Consistent with recent

findings from axisymmetric models, surface entropy fluxes in the eye region of a TC are found to contribute little to the storm intensity while slightly reduce the eye size by lowering the surface pressure in the eye. Although surface entropy fluxes under the eyewall contribute greatly to the storm intensity, those outside the eyewall up to a radius of about 60 km (or about 2-2.5 times the RMW) are also important. Further outward, surface entropy fluxes are found to be critical to the growth of the inner-core size but limit the maximum intensity of a TC.

The dependence of the storm inner-core size on the radial distribution of surface entropy fluxes is understood based on the link between the surface entropy flux and the activity of spiral rainbands in the simulated storms. Surface entropy fluxes outside the eyewall plays a critical role in maintaining active spiral rainbands. Latent heat release in these rainbands is responsible for the inner-core size increase of the TC. A positive feedback (Fig. 15) is identified to explain both the overall outward expansion of wind fields in the control experiment and the small inner-core size of the simulated storms in all sensitivity experiments. In the control experiment (Fig. 15a), surface entropy fluxes outside the eyewall favor the large CAPE and convection, thus the development of spiral rainbands. Diabatic heating in spiral rainbands drives boundary layer inflow outside the eyewall, which accelerates tangential winds through radial advection of angular momentum. This would lead to outward expansion of tangential winds and thus the increase in the inner-core size. This, in turn, may enhance surface fluxes and the outward expansion of relatively high absolute vorticity. The latter would enhance convection in spiral rainbands through Ekman pumping and make the radial advection of angular momentum to

accelerate the tangential winds outside the eyewall more effectively.

In contrast, removal of surface entropy fluxes outside a certain radius outside the eyewall in all sensitivity experiments reduces the CAPE outside the eyewall and suppresses the activity of spiral rainbands and diabatic heating outside the eyewall (Fig. 15b). This greatly reduces the boundary layer inflow, limiting the acceleration of tangential winds outside the RMW due to the reduced radial advection of angular momentum and prohibiting the outward expansion of tangential wind fields. This latter would reduce surface entropy fluxes even within the radius outside of which surface entropy fluxes are removed, further reducing the CAPE outside the eyewall and suppressing spiral rainbands. This is a positive feedback resulting in the contraction of wind fields and the small inner-core size of the storms in all sensitivity experiments.

The activity of spiral rainbands is affected by many factors, including the structure of the initial TC, cloud microphysics, relative humidity in the near core environment, and interactions with vertical shear, synoptic, and mesoscale systems. Detailed studies on these processes would further improve our understanding of TC structure and intensity changes. Some of our preliminary results show that the inner-core size of the simulated storms is determined greatly by the size of the initial model vortex. This can be also explained by the positive feedback processes summarized in Fig. 15 because the size of the initial vortex determines the radial coverage of relatively high absolute vorticity and the radial distribution of surface entropy fluxes. The former is important for the acceleration of tangential winds due to the radial angular momentum transport and the latter is the key to the development of spiral rainbands. Our results suggest that accurate prediction of the inner-core size of TCs is very challenging because the inner-core size is significantly affected by processes in spiral rainbands in addition to the eyewall processes.

Acknowledgments: The authors are grateful to three anonymous reviewers for their constructive review comments. This study has been supported by NSF grant ATM-0754039. Additional support has been provided by the JAMSTEC, NASA, and NOAA through their sponsorships of the International Pacific Research Center (IPRC) in the School of Ocean and Earth Science and Technology (SOEST) at the University of Hawaii.

References

Bell, M. M., and M. T. Montgomery, 2008: Observed structure, evolution, and potential intensity of category 5 Hurricane Isabel from 12 to 14 September. *Mon. Wea. Rev*., **136**, 2023-2046.

Black, P. G., and G. J. Holland, 1995: The boundary layer of Tropical Cyclone Kerry (1979). *Mon. Wea. Rev*., **123**, 2007-2028.

Brand, S., 1972: Very large and very small typhoons of the western North Pacific Ocean. *J. Meteor. Soc. Japan*, **50**, 332-341.

Bryan, G. H., and R. Rotunno, 2009: The influence of near-surface, high-entropy air in hurricane eyes on maximum hurricane intensity. *J. Atmos. Sci*., **66**, 148-158.

Cocks, S. B., and W. M. Gray, 2002: Variability of the outer wind profiles of western North Pacific typhoons: Classifications and techniques for analysis and forecasting. *Mon. Wea. Rev.*, **130**, 1989-2005.

Cram, T. A., J. Persing, M. T. Montgomery, and S. A. Braun, 2007: A Lagrangian trajectory view on transport and mixing processes between the eye, eyewall, and environment using a high-resolution simulation of Hurricane Bonnie (1998). *J. Atmos. Sci*., **64**, 1835-1856.

Demuth, J. L., M. DeMaria, and J. A. Knaff, 2006: Improvement of advanced microwave sounding units tropical cyclone intensity and size estimation algorithms. *J. Appl. Meteor. Climatol.*, **45**, 1573-1581.

Emanuel, K. A., 1986: An air-sea interaction theory of tropical cyclones. Part I: Steady-state maintenance. *J. Atmos. Sci*., **43**, 585-604.

Emanuel, K. A., 1995: Sensitivity of tropical cyclones to surface exchange coefficients and a revised steady-state model incorporating eye dynamics. *J. Atmos. Sci*., **52**, 3969-3676.

Emanuel, K. A., 1997: Some aspects of hurricane inner-core dynamics and energetic. *J. Atmos.*

Sci., **54**, 1014-1026.

Fairall, C. W., E. F. Bradley, J. E. Hare, A. A. Grachev, and J. B. Edson, 2003: Bulk parameterization of air–sea fluxes: Updates and verification for the COARE algorithm. *J. Climate,* **16**, 571–591.

Gray, W. M., E. Ruprecht and R. Phelps, 1975: Relative humidity in tropical weather systems. *Mon. Wea. Rev.*, **103**, 685-690.

Harr, P. A., M. R. Kalafsky, and R. Elsberry, 1996: Environmental conditions prior to formation of a midget tropical cyclone during TCM-93. *Mon. Wea. Rev*., **124**, 1693-1710.

Hill, K. A., and G. M. Lackmann, 2009: Influence of environmental humidity on tropical cyclone size. *Mon. Wea. Rev*., **137**, 3294-3315.

Holland, G. J., and R. T. Merrill, 1984: On the dynamics of tropical cyclone structure changes. *Q. J. Roy. Meteor. Soc*., **110**, 723-745.

Kimball, S. K., and M. S. Mulekar, 2004: A 15-year climatology of North Atlantic tropical cyclones: Part I: Size parameters. *J. Climate*, **17**, 3555-3575.

Knaff, J.A., J.P. Kossin, and M. DeMaria, 2003: Annular hurricanes. *Wea. Forecasting*, **18**, 204-223.

Knaff, J.A., C. R. Sampson, M. DeMaria, T. P. Marchok, J. M. Gross, and C. J. McAdie, 2007: Statistical tropical cyclone wind radii prediction using climatology and persistence. *Wea. Forecasting*, **22**, 781-791.

Kossin, J. P., J. A. Knaff, H. I. Berger, D. C. Hendon, T. A. Cram, C. S. Velden, R. J. Murnane, and J. D. Hawkins, 2007: Estimating hurricane wind structure in the absence of aircraft reconnaissance. *Wea. Forecasting*, **22**, 89-101.

Langland, R. H., and C.-S. Liou, 1996: Implementation of an E-ε parameterization of vertical

subgrid-scale mixing in a regional model. *Mon. Wea. Rev.*, **124**, 905-918.

Maclay, K. S., M. DeMaria, and T. H. V. Haar, 2008: Tropical cyclone inner-core kinetic energy evolution. *Mon. Wea. Rev*., **136**, 4882-4898.

Malkus, J. S., and H. Riehl, 1960: On the dynamics and energy transformations in steady-state hurricane. *Tellus*, **12**, 1-20.

May, P. T., G. J. Holland, 1999: The role of potential vorticity generation in tropical cyclone rainbands. *J. Atmos. Sci.*, **56**, 1224-1228.

Merrill, R. T., 1984: A comparison of large and small tropical cyclones. *Mon. Wea. Rev*., **112**, 1408-1418.

Montgomery, M. T., M. M. Bell, S. D. Aberson, and M. L. Black, 2006: Hurricane Isabel (2003): New insights into the physics of intense storm. Part I: Mean vortex structure and maximum intensity estimates. *Bull. Amer. Meteor. Soc*., **87**, 1335-1347.

Moyer, A. C., J. L. Evans, and M. Powell, 2007: Comparison of observed gale radius statistics. *Meteor. Atmos. Phys*., **97**, 41-55.

Ooyama, K. V., 1969: Numerical simulation of the life cycle of tropical cyclones. *J. Atmos. Sci.*, **26**, 3-40.

Ooyama, K. V., 1982: Conceptual evolution of the theory and modeling of the tropical cyclones. *J. Meteor. Soc. Japan*, **60**, 364-380.

Persing, J., and M.T. Montgomery, 2003: Hurricane superintensity. *J. Atmos. Sci.*, **60**, 2349-2371.

Persing, J., and M. T. Montgomery, 2005: In environmental CAPE important in the determination of maximum possible hurricane intensity? *J. Atmos. Sci*., **62**, 542-550.

Rotunno, R., and K. A. Emanuel, 1987: An air-sea interaction theory for tropical cyclones. Part

II: Evolutionary study using a non-hydrostatic axisymmetric model. *J. Atmos. Sci*, **44,** 542-561.

Rozoff, C.M., W.H. Schubert, B.D. McNoldy, and J.P. Kossin, 2006: Rapid filamentation zones in intense tropical cyclones. *J. Atmos. Sci*., **63**, 325-340.

Schubert, W. H., M. T. Montgomery, R. K. Taft, T. A. Guinn, S. R. Fulton, J. P. Kossin, and J. P. Edwards, 1999: Polygonal eyewalls, asymmetric eye contraction, and potential vorticity mixing in hurricanes. *J. Atmos. Sci*., **56**, 1197-1223.

Smith, R. K., M. T. Montgomery, and S. V. Nyuyen, 2009: Tropical cyclone spin-up revisited. *Q. J. R. Meteorol. Soc*.**135**, 1321-1335.

Wang, Y., 2001: An explicit simulation of tropical cyclones with a triply nested movable mesh primitive equation model: TCM3. Part I: Model description and control experiment. *Mon. Wea. Rev*., **129,** 1370-1394.

Wang, Y., 2002a: Vortex Rossby waves in a numerically simulated tropical cyclone. Part I: Overall structure, potential vorticity and kinetic energy budgets. *J. Atmos. Sci.,* **59**, 1213-1238.

Wang, Y., 2002b: Vortex Rossby waves in a numerically simulated tropical cyclone. Part II: The role in tropical cyclone structure and intensity changes. *J. Atmos. Sci.,* **59**, 1239-1262.

Wang, Y., 2002c: An explicit simulation of tropical cyclones with a triply nested movable mesh primitive equation model-TCM3 Part II: Model refinements and sensitivity to cloud microphysics parameterization. *Mon. Wea. Rev.*, **130**, 3022-3036.

Wang, Y., 2007: A multiply nested, movable mesh, fully compressible, nonhydrostatic tropical cyclone model - TCM4: Model description and development of asymmetries without explicit asymmetric forcing. *Meteor. Atmos. Phys*., 97, 93-116.

Wang, Y., 2008a: Rapid filamentation zone in a numerically simulated tropical cyclone. *J. Atmos. Sci.*, **65**, 1158-1181.

Wang, Y., 2008b, Structure and formation of an annular hurricane simulated in a fully compressible, nonhydrostatic model–TCM4. *J. Atmos. Sci.*, **65**, 1505-1527.

Wang, Y., 2009: How do outer spiral rainbands affect tropical cyclone structure and intensity? *J. Atmos. Sci.*, **66**, 1250-1273.

Wang, Y., and J. Xu, 2010: Energy production, frictional dissipation, and maximum intensity of a numerically simulated tropical cyclone. *J. Atmos. Sci*., **67**, 97-116.

Weatherford, C. L., and W. M. Gray, 1988a: Typhoon structure as revealed by aircraft reconnaissance. Part I: Data analysis and climatology. *Mon. Wea. Rev*., **116**, 1032-1043.

Weatherford, C. L., and W. M. Gray, 1988b: Typhoon structure as revealed by aircraft reconnaissance. Part II: Structural variability. *Mon. Wea. Rev*., **116**, 1044-1056.

Willoughby, H. E., J. A. Clos, and M. G. Shoreibah, 1982: Concentric eye walls, secondary wind maxima, and the evolution of the hurricane vortex. *J. Atmos. Sci*., **39**, 395-411.

Willoughby, H. E., F. D. Marks, and R. J. Feinberg, 1984: Stationary and moving convective bands in hurricanes. *J. Atmos. Sci*., **41**, 3189-3211.

Yang, B., Y. Wang, and B. Wang, 2007: The effect of internally generated inner-core asymmetries on tropical cyclone potential intensity. *J. Atmos. Sci*., **64**, 1165-1188.

Figure captions

Figure 1. Axisymmetric structure of the simulated tropical cyclone after 48 h of spinup with standard model settings. (a) Tangential wind speed (m s^{-1}), (b) radial wind speed (m s^{-1}), (c) vertical wind speed (m s^{-1}), (d) perturbation temperature (K), (e) potential vorticity (PVU), and (f) equivalent potential temperature (K).

Figure 2. Time evolution of (a) the maximum azimuthal mean wind speed (m s^{-1}) at the lowest model level (35.6 m above the sea surface) and (b) the minimum sea level pressure (hPa) in experiments CTRL, IE1, and IE2 as described in Table 1.

Figure 3. Radial-height cross-section of the azimuthal mean equivalent potential temperature (K, shading), tangential wind (m s^{-1}, white contours), and vertical velocity (m s^{-1}, black contours) at given times or time mean in experiments CTRL, IE1, and IE2 as described in Table 1 .

Figure 4. Radius-time cross-section of the azimuthal mean equivalent potential temperature (K, shading) and tangential wind speed (m s^{-1}, contours of 50, 55, 60, and 65 m s^{-1}) at the lowest model level (35.6 m above the sea surface) from experiments: (a) CTRL, (b) IE1 and (c) IE2 as described in Table 1.

Figure 5. The radial distributions of the azimuthal mean tangential wind (a), radial wind (b), equivalent potential temperature (c), and potential vorticity in PVU (d) at the lowest model level (about 35.6 m above the sea surface) averaged between 168 and 192 h of simulation in experiments CTRL, IE1, and IE2 as described in Table 1.

Figure 6. Time evolution of (a) the maximum azimuthal mean wind speed (m s^{-1}) at the lowest model level (35.6 m above the sea surface) and (b) the minimum sea level pressure (hPa) in experiments CTRL, OE30, OE45, OE60, OE75, OE90, and OE120 as described in Table 1.

Figure 7. Radius-time cross-sections of the azimuthal mean tangential wind speed at the lowest model level (m s^{-1}, shading) and its isotaches of 25.7 m s^{-1} (black contours), and vertical velocity at 5 km height (m s^{-1}, contours with contour interval of 1 m s^{-1}) in experiments (a) CTRL, (b) OE30, (c) OE45, (d) OE60, (e) OE75, and (f) OE120.

Figure 8. The plan view of the rain rate (mm h^{-1}) in the model tropical cyclones after 48 h of

simulation (a) and 144 h of simulation (b) from experiments CTRL, OE30, OE45, OE60, OE75 and OE120. Contours show the isotach of 25.7 m s^{-1} at the lowest model level.

Figure 9. Time evolution of the radius of the azimuthal mean damaging wind (25.7 m s^{-1}, a), the azimuthal mean kinetic energy (b) and surface entropy flux (c) integrated within 150 km radius in experiments CTRL, OE30, OE45, OE60, OE75, OE90, and OE120 as described in Table 1.

Figure 10. Radial distribution of the azimuthal mean (a) tangential wind (m s^{-1}), (b) radial wind (m s^{-1}), (c) equivalent potential temperature (K), and (d) potential vorticity (PVU) after 144 h of simulation in experiments CTRL, OE30, OE45, OE60, OE85, and OE120.

Figure 11. Radius-time cross-section of the azimuthal mean PV (PVU, shading) and total eddy kinetic energy (m^2 s^{-2}, white contours) averaged in the model lowest 3 km layer in experiments (a) CTRL, (b) OE30, (c) OE45, (d) OE60, (e) OE75, and (f) OE120.

Figure 12. Radius-time cross-section of the azimuthal mean rain rate (mm h^{-1}, shading) and CAPE (J kg^{-1}, contours) in experiments (a) CTRL, (b) OE30, (c) OE45, (d) OE60, (e) OE75, and (f) OE120.

Figure 13. Azimuthal mean pressure deficit (in hPa) from the unperturbed environment (a and b) and the corresponding radial pressure gradient (in 10^{-2} m s^{-2}, c and d) at the sea surface averaged between 24 and 48 h (a and c) and between 120 and 168 h (b and d) of integrations in experiments CTRL, OE60, and OE120.

Figure 14. Azimuthal mean acceleration of radial wind (10^{-2} m s^{-2}, a and b), tendency of azimuthal mean tangential wind due to radial advection of absolute angular momentum ($-\overline{u}\overline{\varsigma}_a$, 10^{-2} m s^{-2}, c and d), and the azimuthal mean absolute vorticity (10^{-3} s^{-1}, e and f) at the lowest model level averaged between 24 and 72 h (a, c, and e) and between 120 and 168 h (b, d, and f) of integrations in experiments CTRL, OE60, and OE120.

Figure 15. Schematic diagram showing the positive feedbacks that are responsible for the increase in the inner-core size of the simulated TC in the control experiment (a) and the decrease in the inner-core size for the simulated TCs in all OEs (b). See text for details.

List of Tables

Table 1. Summary of the numerical experiments performed in this study. V_{max} is the lifetime maximum azimuthal-mean tangential wind at the lowest model level in each simulation. RMW shown in the last column is the radius of maximum wind at the lowest model level averaged in the last 24 h in each simulation. r_m is the radius of maximum wind and r is the radial distance from the storm center in kilometers. C_E is the surface exchange coefficient in the model.

Experiment	Modification to the exchange coefficient for surface entropy flux	V_{max} (m s^{-1})	r_m (km)
CTRL	Control experiment	70	25
IE1	$C_E = 0$ for $r \le r_m$	63	30
IE2	$C_E = 0$ for $r \le 0.8 * r_m$	67	27.5
OE30	C_E decreases to zero linearly from r = 30 km to r = 45 km	60	7.5
OE45	C_E decreases to zero linearly from r = 45 km to r = 60 km	67	7.5
OE60	C_E decreases to zero linearly from r = 60 km to r = 75 km	71	7.5
OE75	C_E decreases to zero linearly from r = 75 km to r = 90 km	72	7.5
OE90	C_E decreases to zero linearly from r = 90 km to r = 120 km	72	10
OE120	C_E decreases to zero linearly from r = 120 km to r = 150 km	73	10

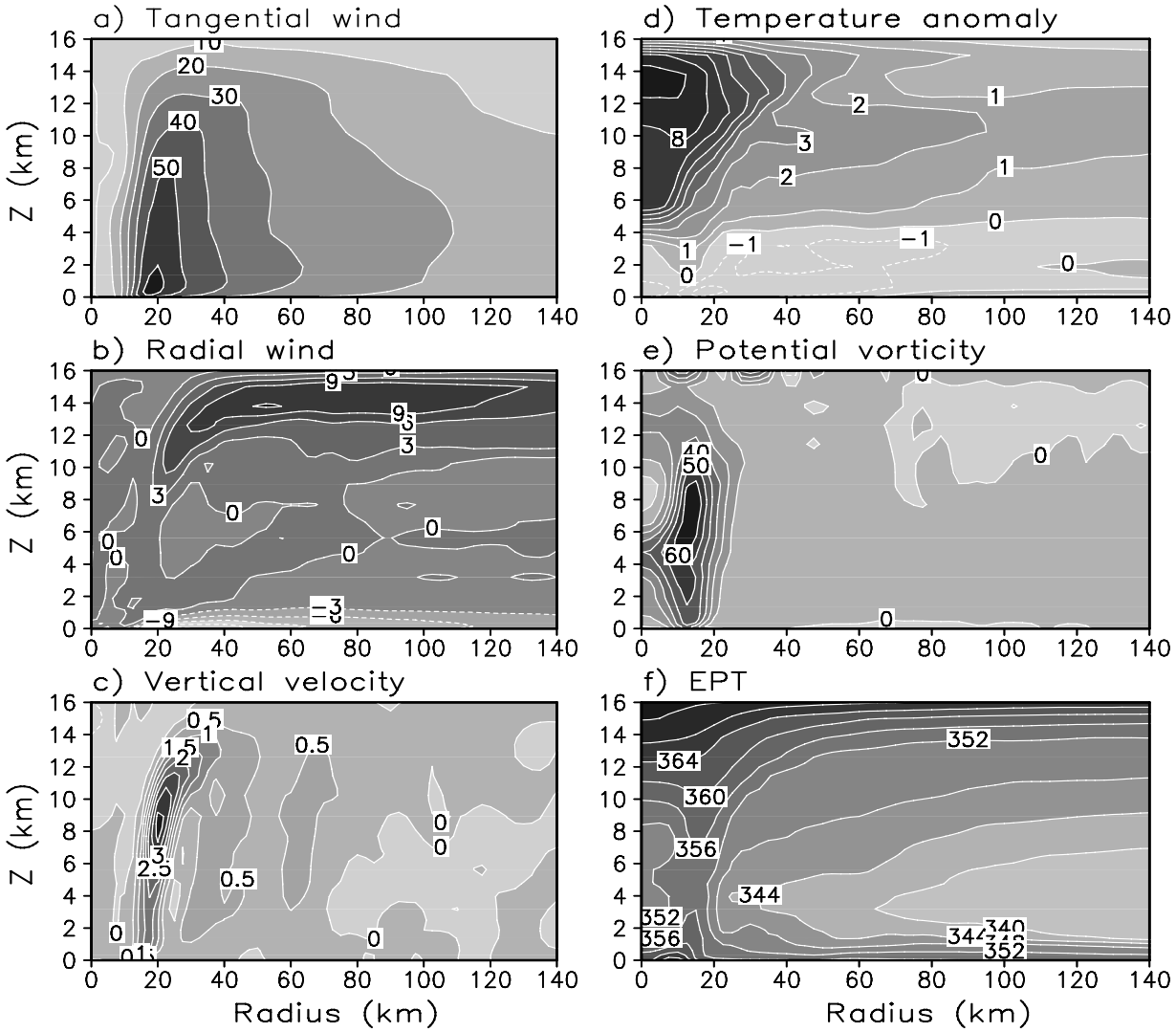

Figure 1. Axisymmetric structure of the simulated tropical cyclone after 48 h of spinup with standard model settings. (a) Tangential wind speed (m s^{-1}), (b) radial wind speed (m s^{-1}), (c) vertical wind speed (m s^{-1}), (d) perturbation temperature (K), (e) potential vorticity (PVU), and (f) equivalent potential temperature (K).

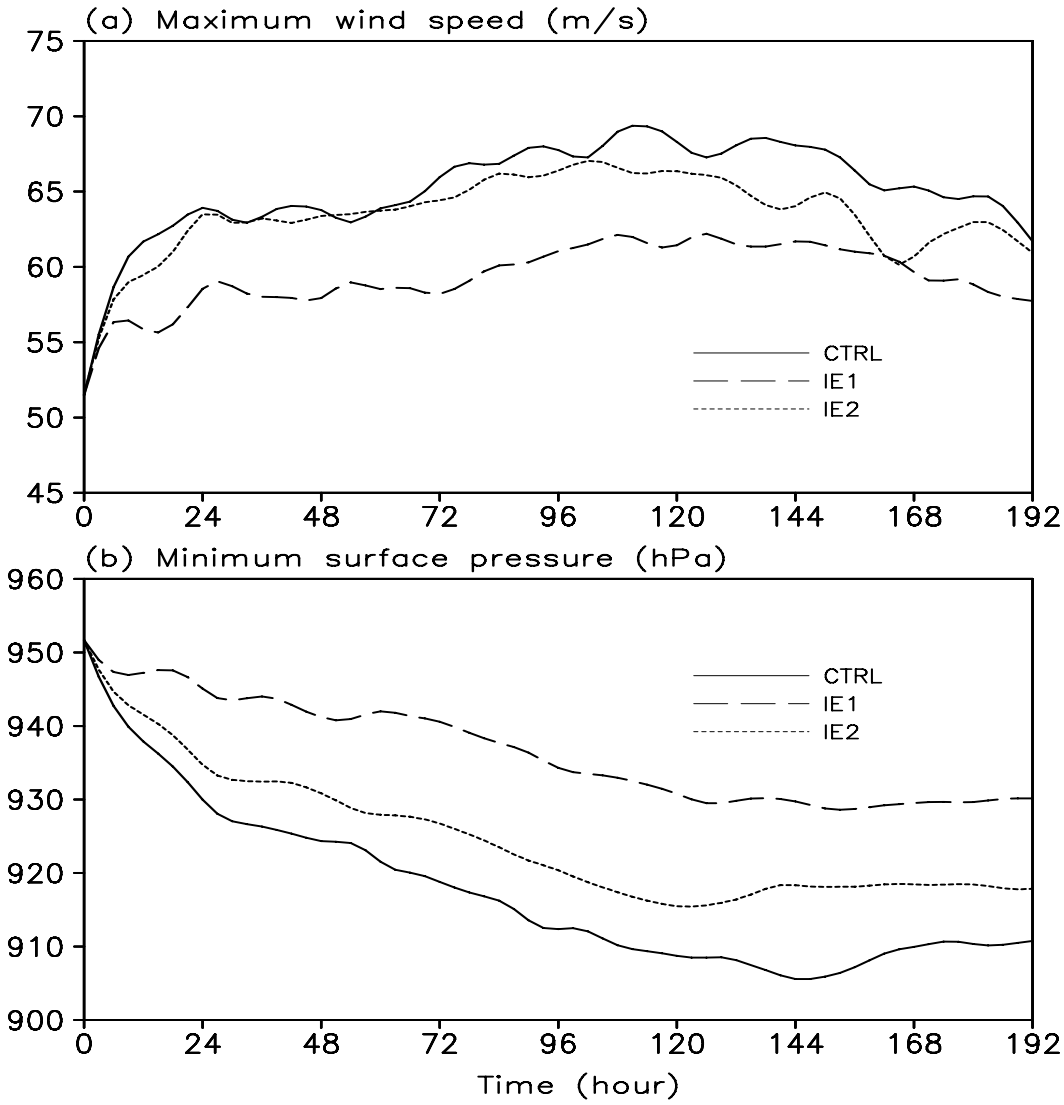

Figure 2. Time evolution of (a) the maximum azimuthal mean wind speed (m s^{-1}) at the lowest model level (35.6 m above the sea surface) and (b) the minimum sea level pressure (hPa) in experiments, IE1, and IE2 as described in Table 1.

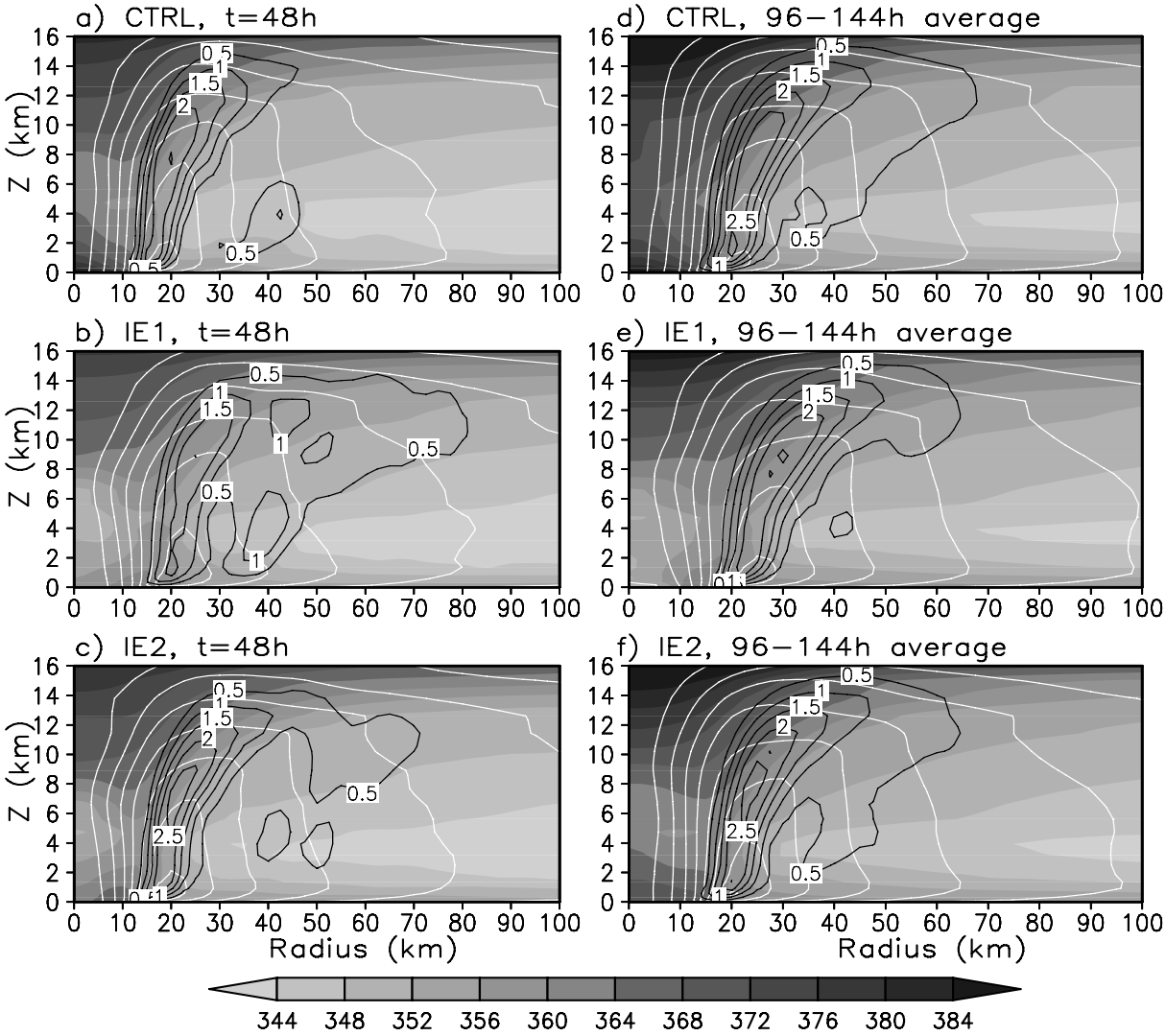

Figure 3. Radial-height cross-section of the azimuthal mean equivalent potential temperature (K, shading), tangential wind (m s^{-1}, white contours), and vertical velocity (m s^{-1}, black contours) at given times or time mean in experiments CTRL, IE1, and IE2 as described in Table 1.

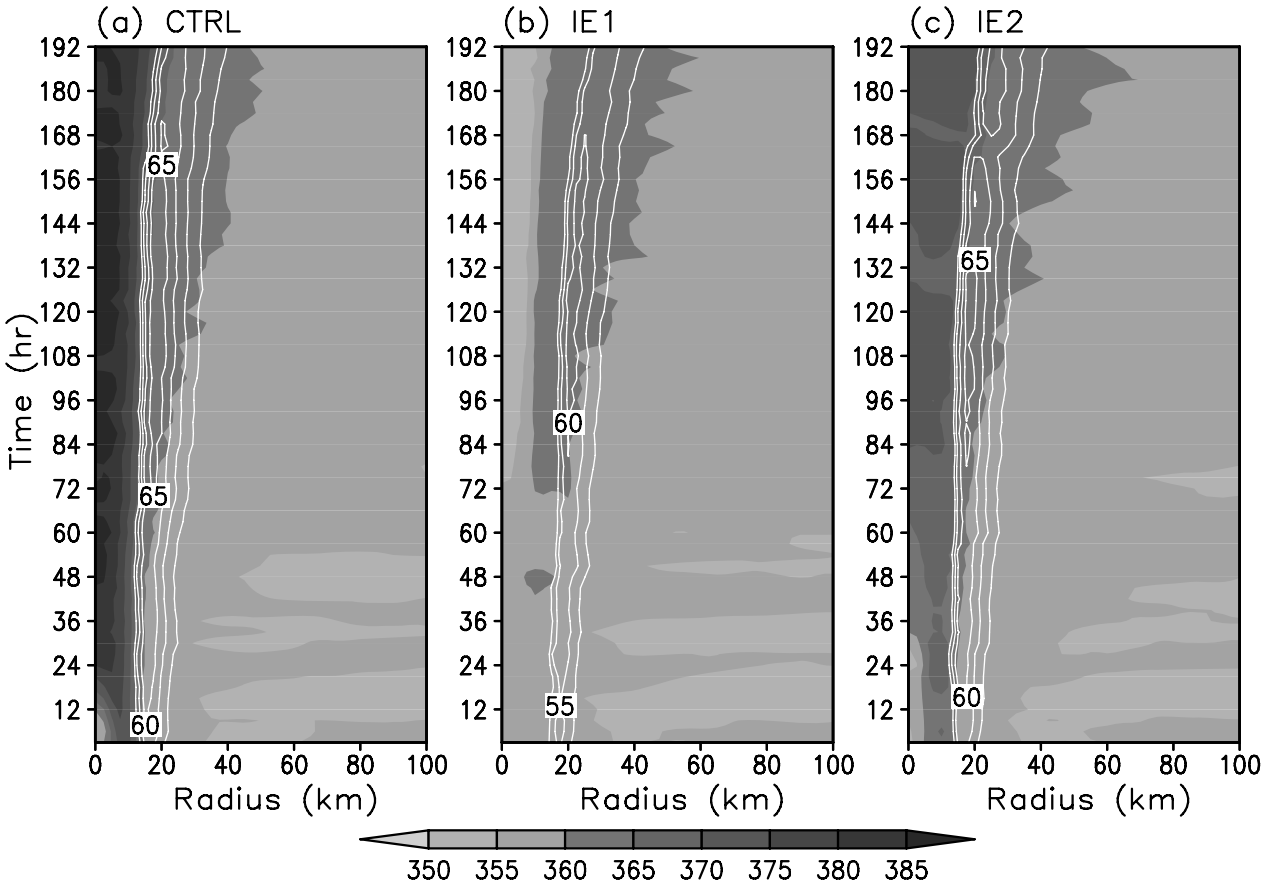

Figure 4. Radius-time cross-section of the azimuthal mean equivalent potential temperature (K, shading) and tangential wind speed (m s^{-1}, contours of 50, 55, 60, and 65 m s^{-1}) at the lowest model level (35.6 m above the sea surface) from experiments: (a) CTRL, (b) IE1 and (c) IE2 as described in Table 1.

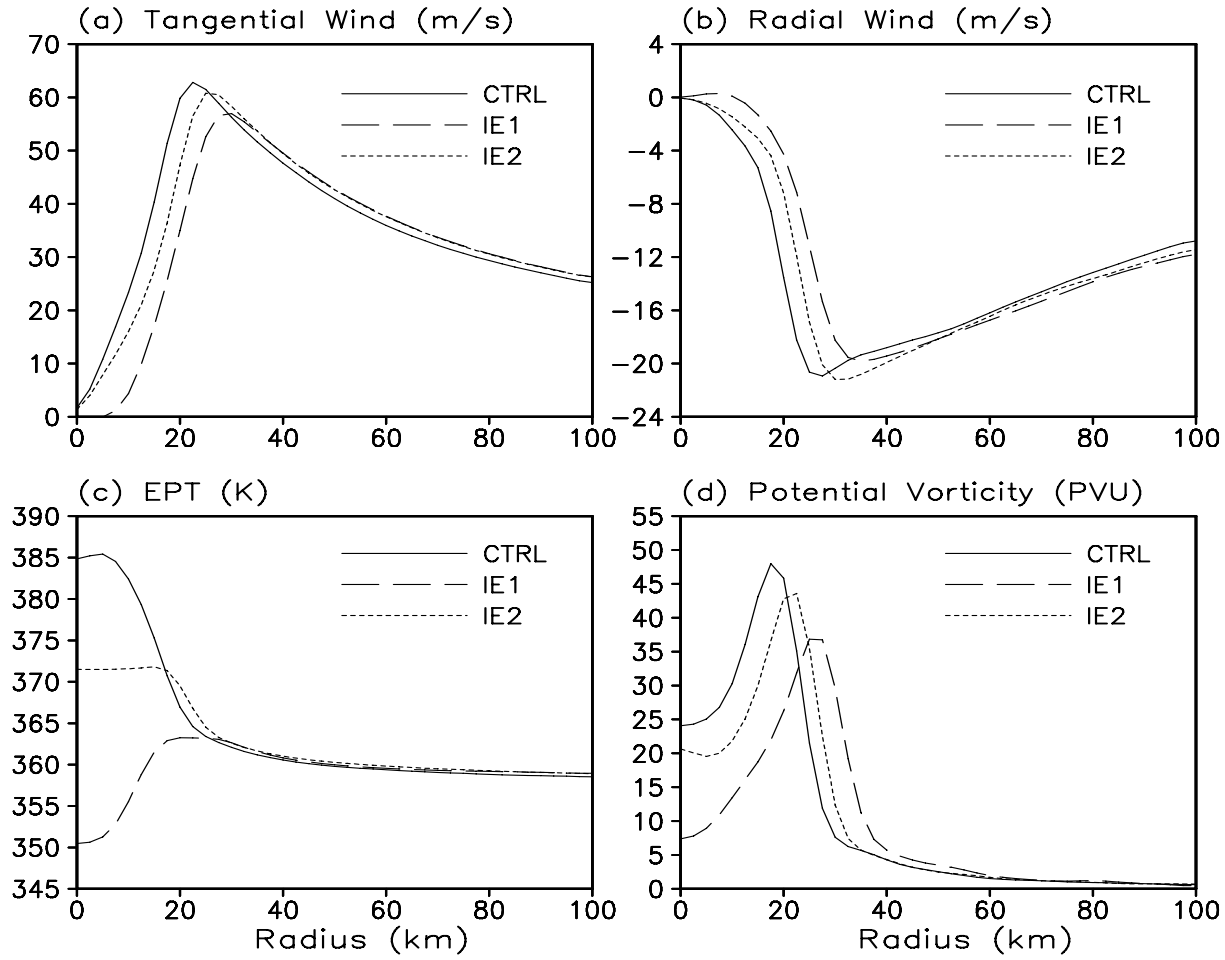

Figure 5. The radial distributions of the azimuthal mean tangential wind (a), radial wind (b), equivalent potential temperature (c), and potential vorticity in PVU (d) at the lowest model level (35.6 m above the sea surface) averaged between 168 and 192 h of simulation in experiments CTRL, IE1, and IE2 as described in Table 1.

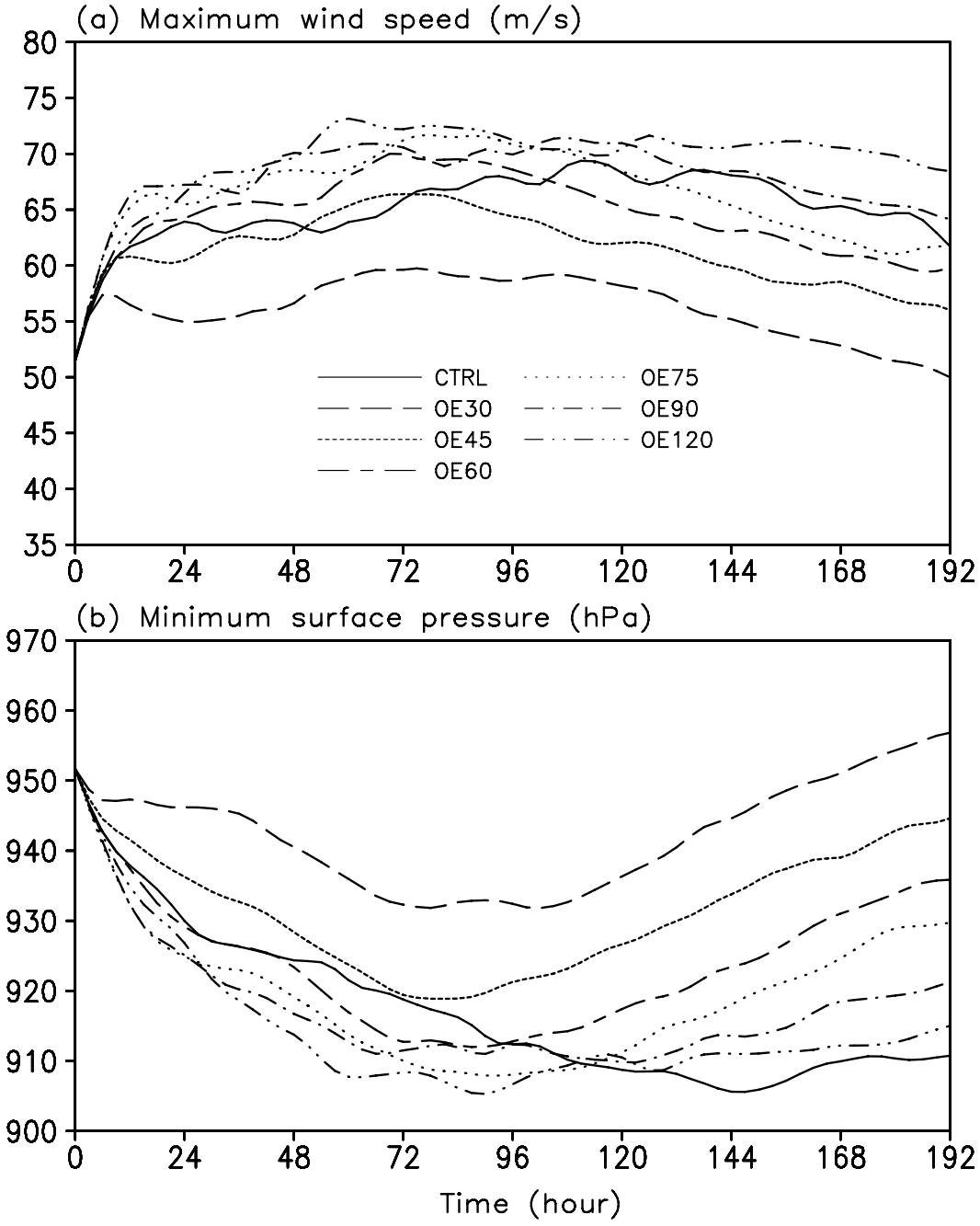

Figure 6. Time evolution of (a) the maximum azimuthal mean wind speed (m s^{-1}) at the lowest model level (35.6 m above the sea surface) and (b) the minimum sea level pressure (hPa) in experiments CTRL, OE30, OE45, OE60, OE75, OE90, and OE120 as described in Table 1.

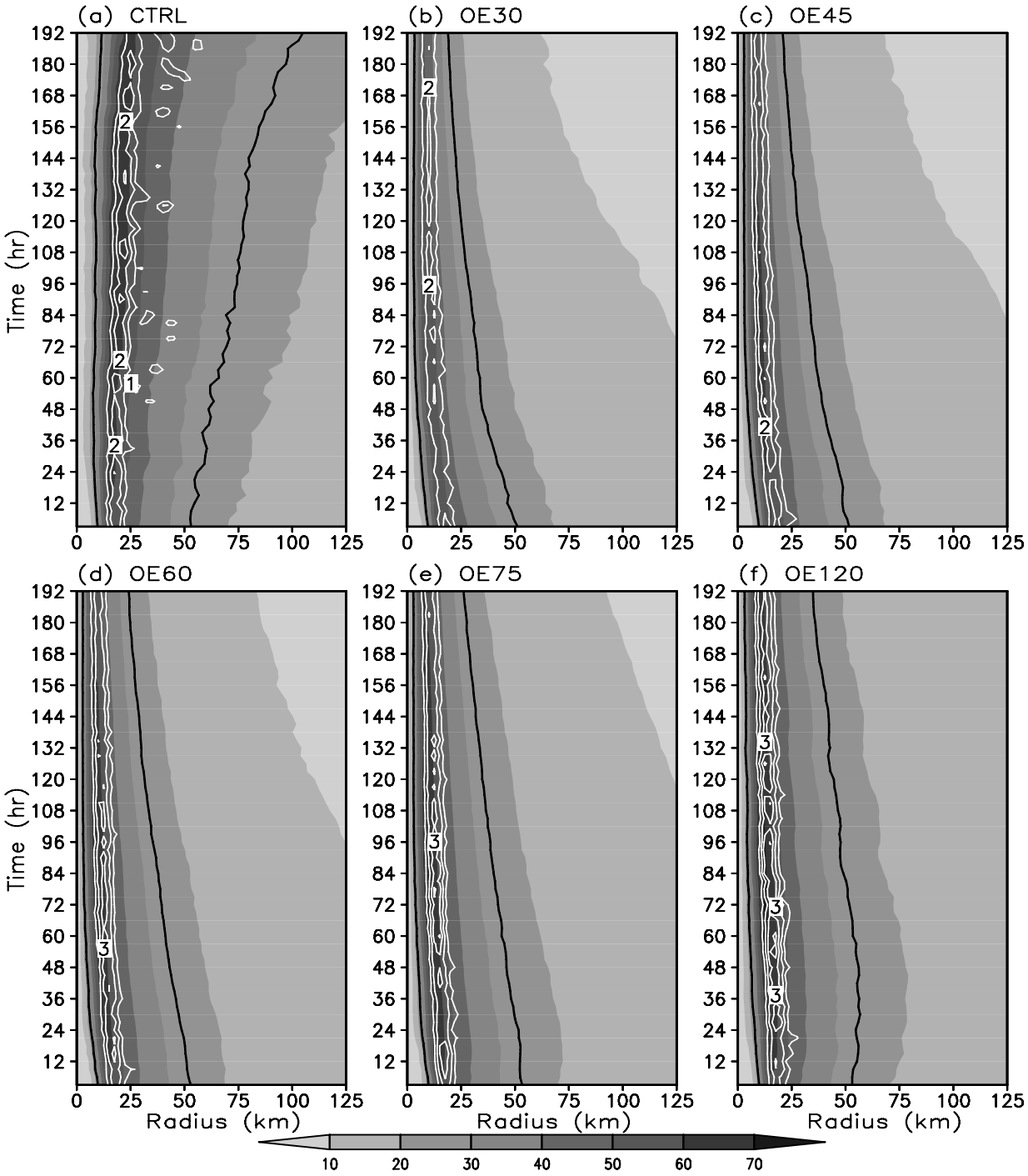

Figure 7. Radius-time cross-sections of the azimuthal mean tangential wind speed at the lowest model level (m s^{-1}, shading) and its isotaches of 25.7 m s^{-1} (black contours), and vertical velocity at 5 km height (m s^{-1}, white contours with contour interval of 1 m s^{-1}) in experiments (a) CTRL, (b) OE30, (c) OE45, (d) OE60, (e) OE75, and (f) OE120.

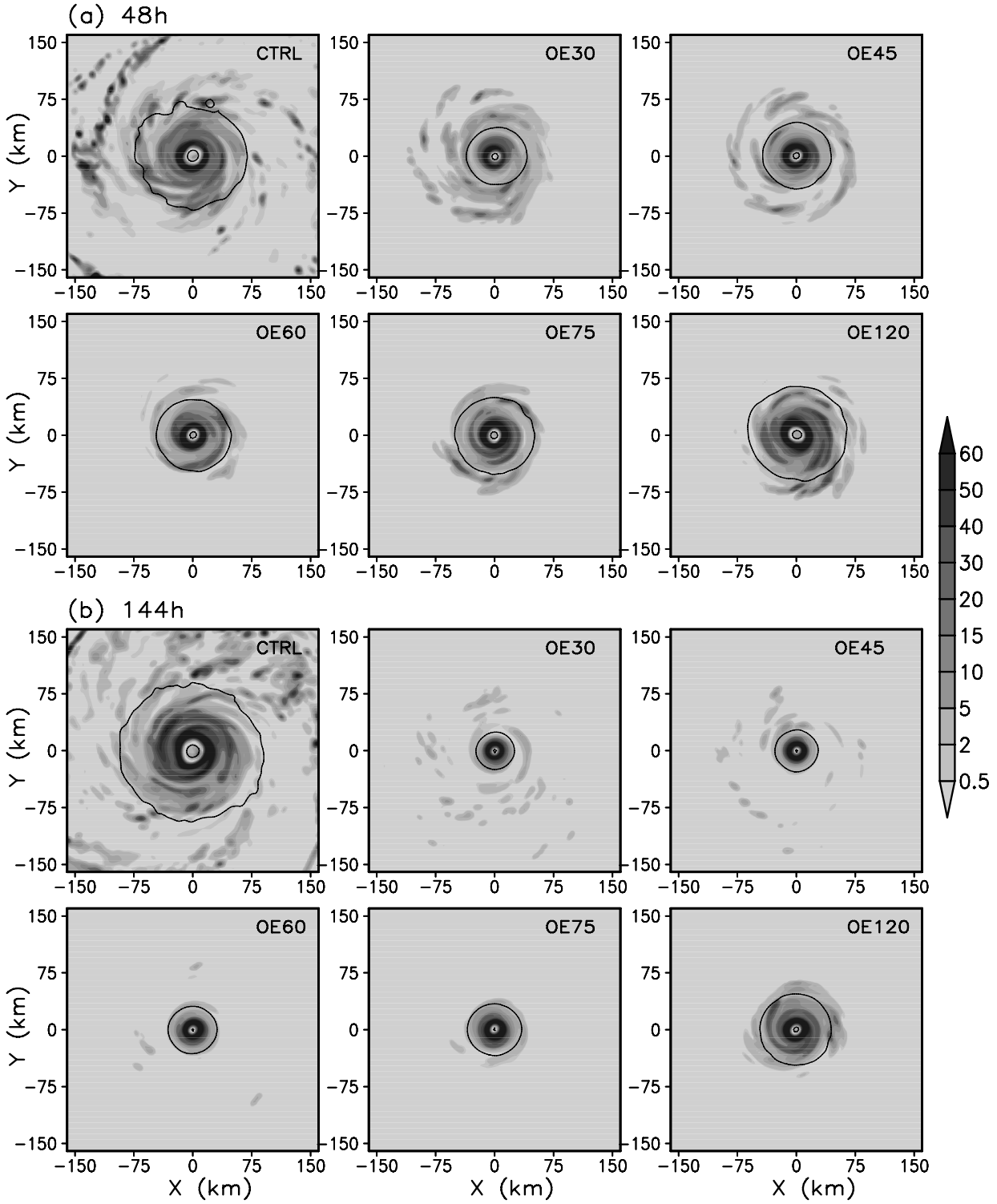

Figure 8. The plan view of the rain rate (mm h^{-1}) in the model tropical cyclones after 48 h of simulation (a) and 144 h of simulation (b) from experiments CTRL, OE30, OE45, OE60, OE75 and OE120. Contours show the isotach of 25.7 m s^{-1} at the lowest model level.

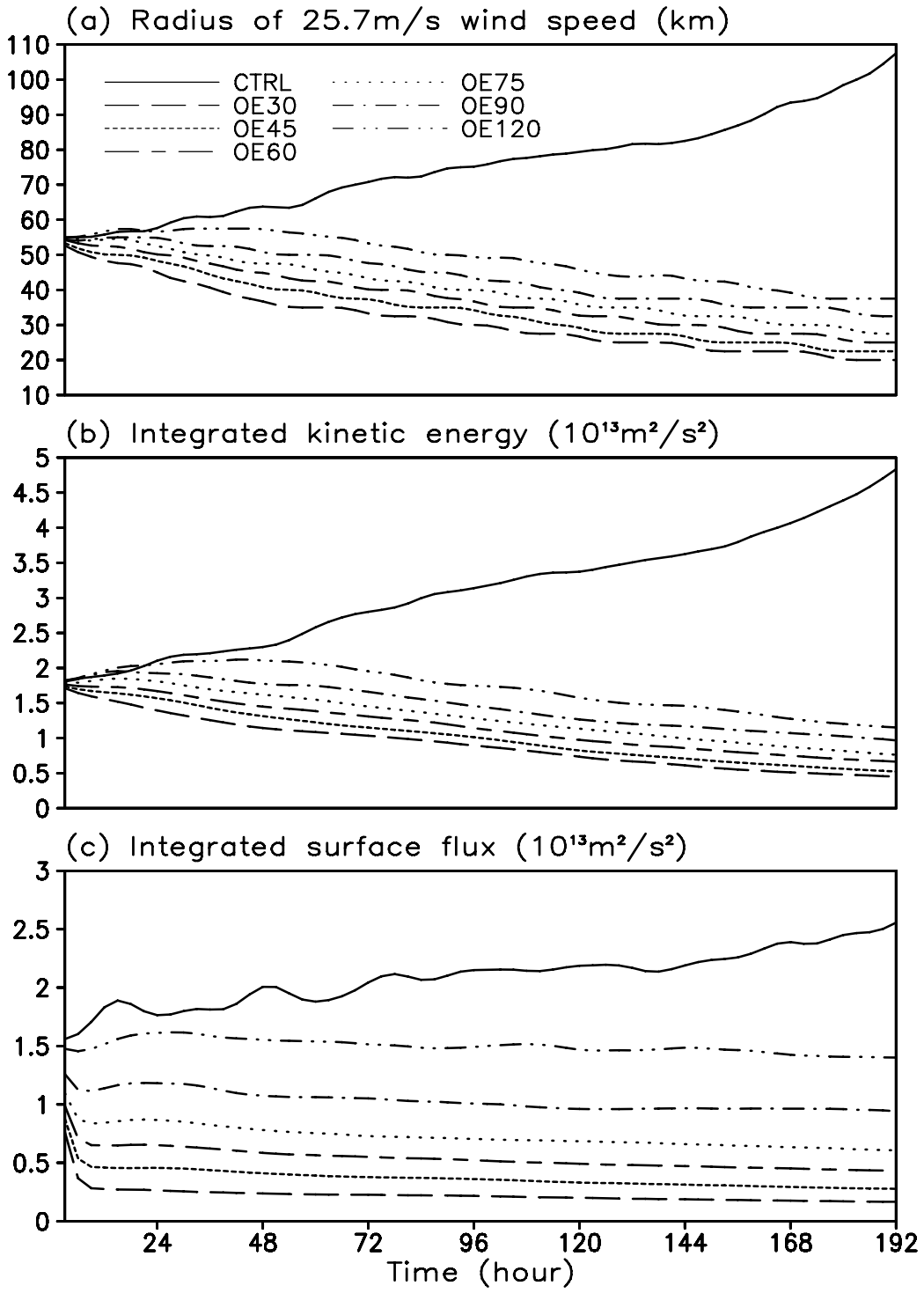

Figure 9. Time evolution of the radius of the azimuthal mean damaging wind (25.7 m s^{-1}, a), the azimuthal mean kinetic energy (b) and surface entropy flux (c) integrated within 150 km radius in experiments CTRL, OE30, OE45, OE60, OE75, OE90, and OE120 as described in Table 1.

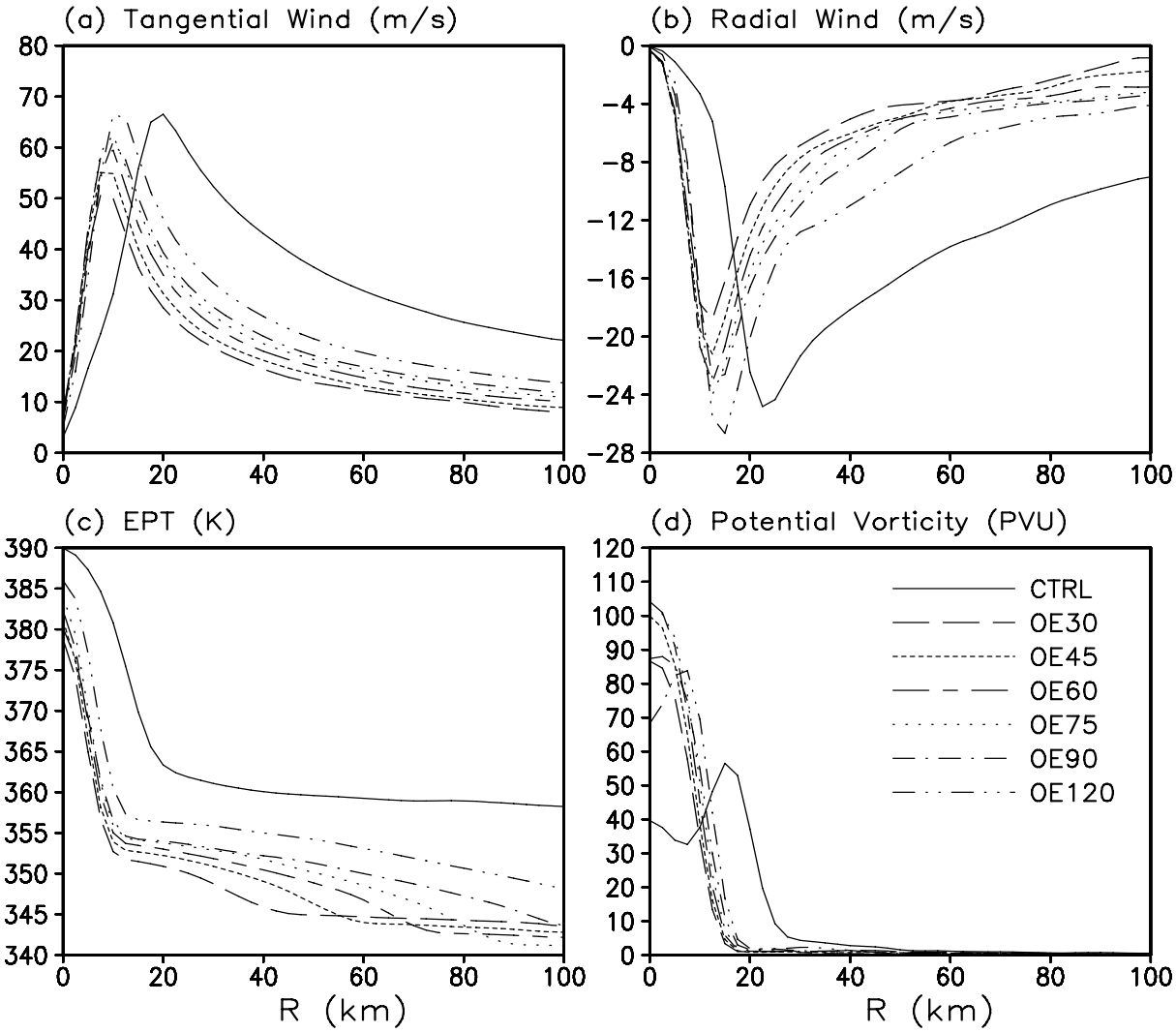

Figure 10. Radial distribution of the azimuthal mean (a) tangential wind (m s^{-1}), (b) radial wind (m s^{-1}), (c) equivalent potential temperature (K), and (d) potential vorticity (PVU) after 144 h of simulation in experiments CTRL, OE30, OE45, OE60, OE75, OE90, and OE120.

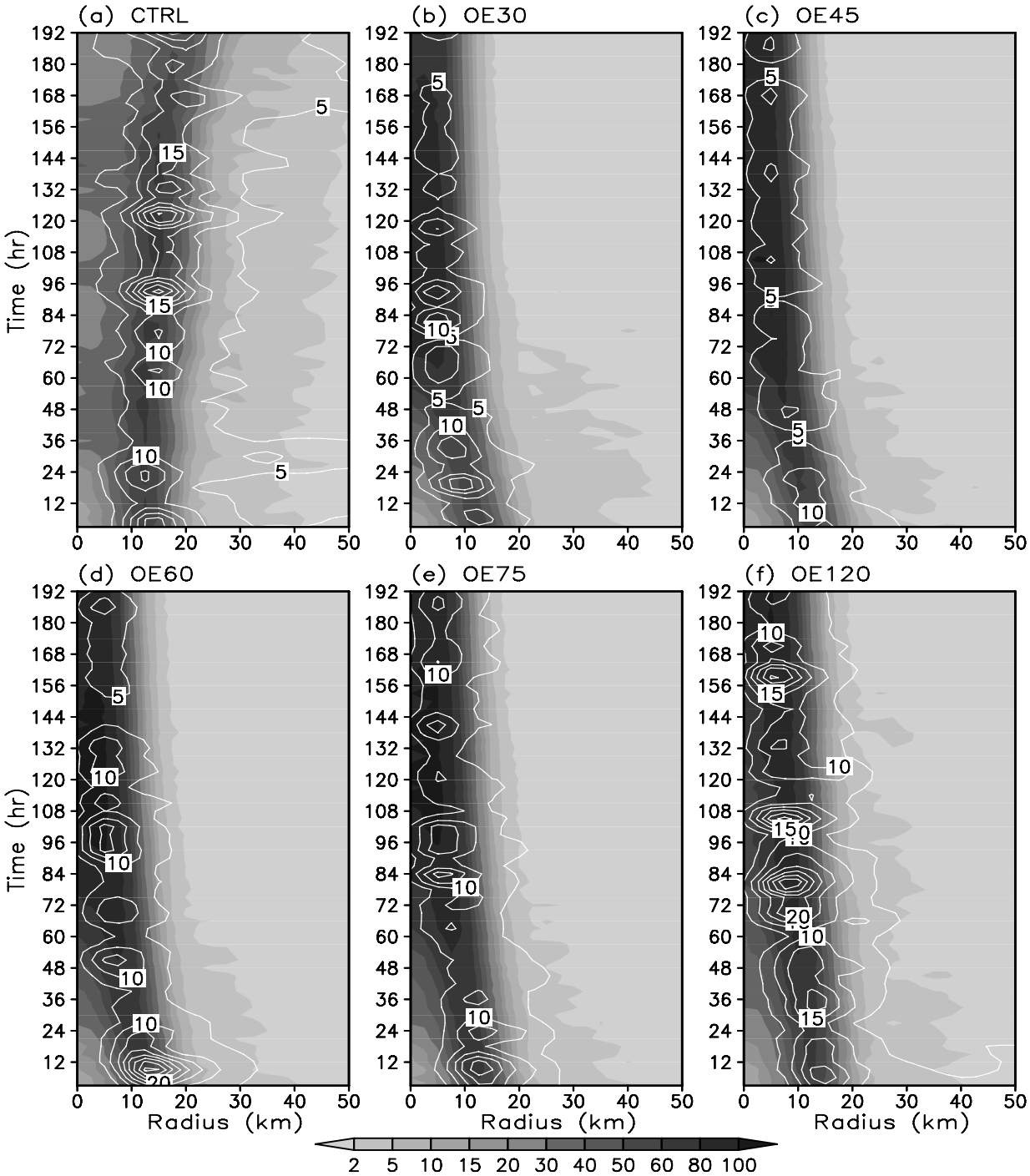

Figure 11. Radius-time cross-section of the azimuthal mean PV (PVU, shading) and total eddy kinetic energy (m^2 s^{-2}, white contours) averaged in the model lowest 3 km layer in experiments (a) CTRL, (b) OE30, (c) OE45, (d) OE60, (e) OE75, and (f) OE120.

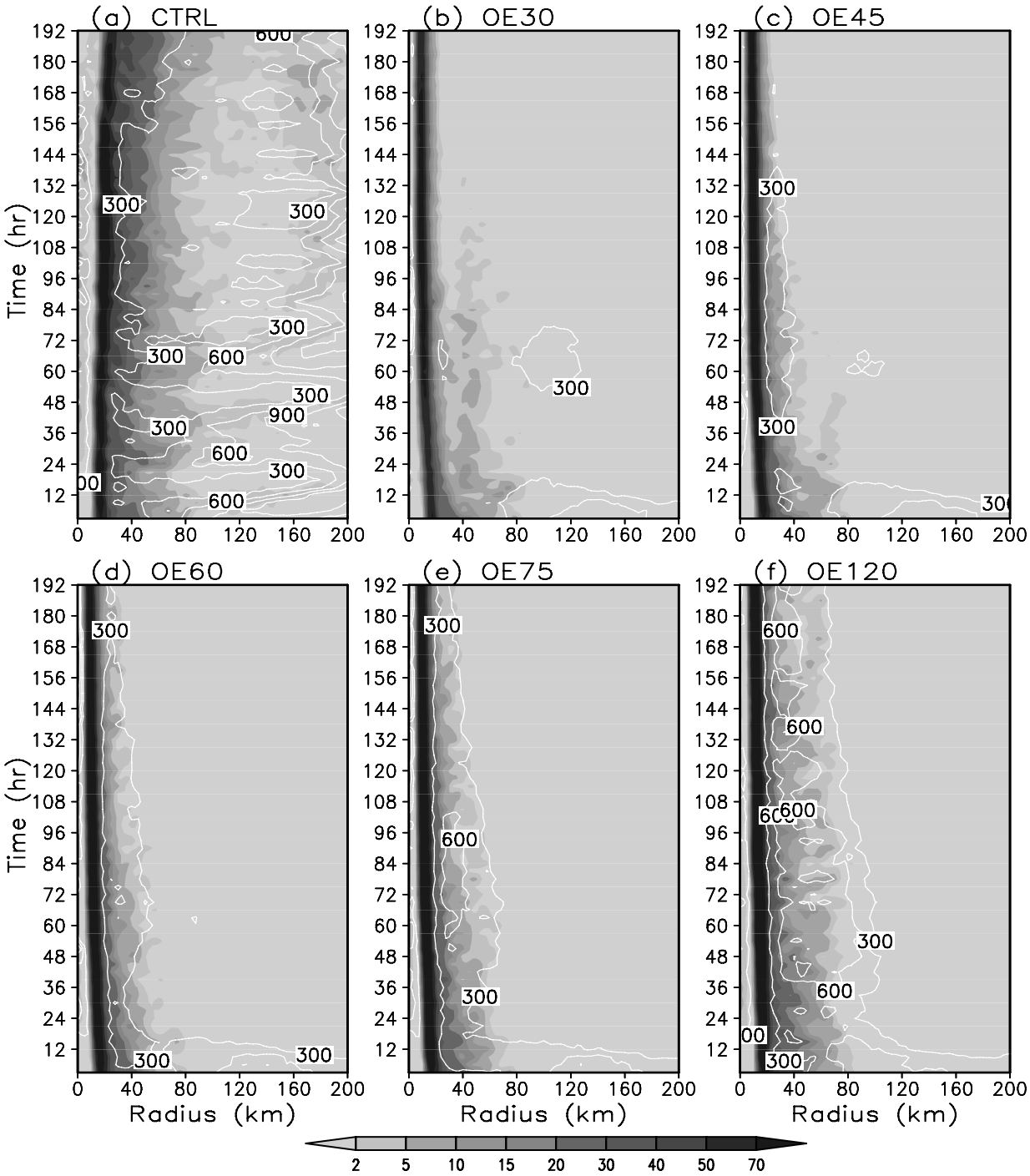

Figure 12. Radius-time cross-section of the azimuthal mean rain rate (mm h^{-1}, shading) and CAPE (J kg^{-1}, contours) in experiments (a) CTRL, (b) OE30, (c) OE45, (d) OE60, (e) OE75, and (f) OE120.

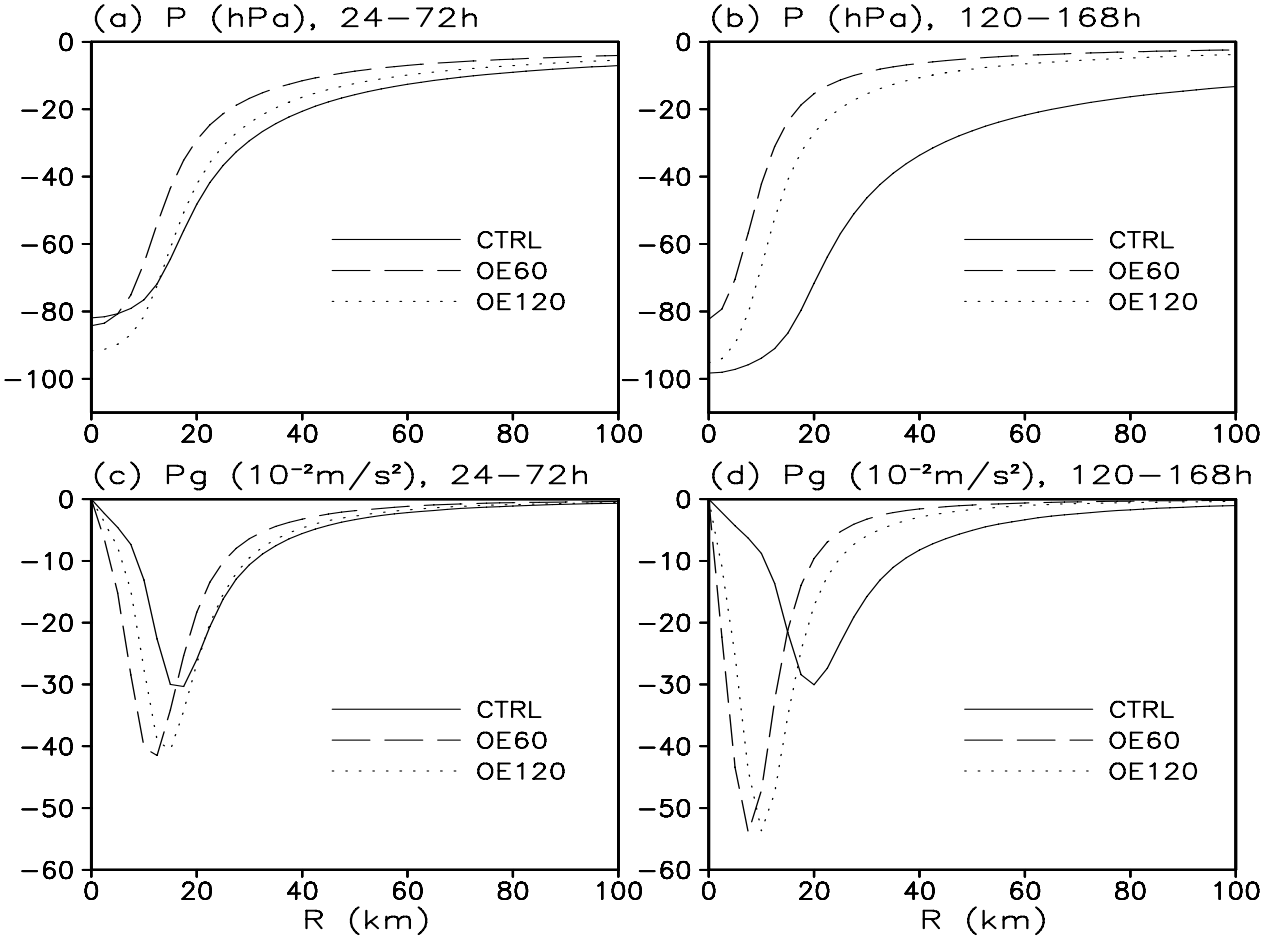

Figure 13. Azimuthal mean pressure deficit (in hPa) from the unperturbed environment (a and b) and the corresponding radial pressure gradient (in 10^{-2} m s^{-2}, c and d) at the sea surface averaged between 24 and 48 h (a and c) and between 120 and 168 h (b and d) of integrations in experiments CTRL, OE60, and OE120.

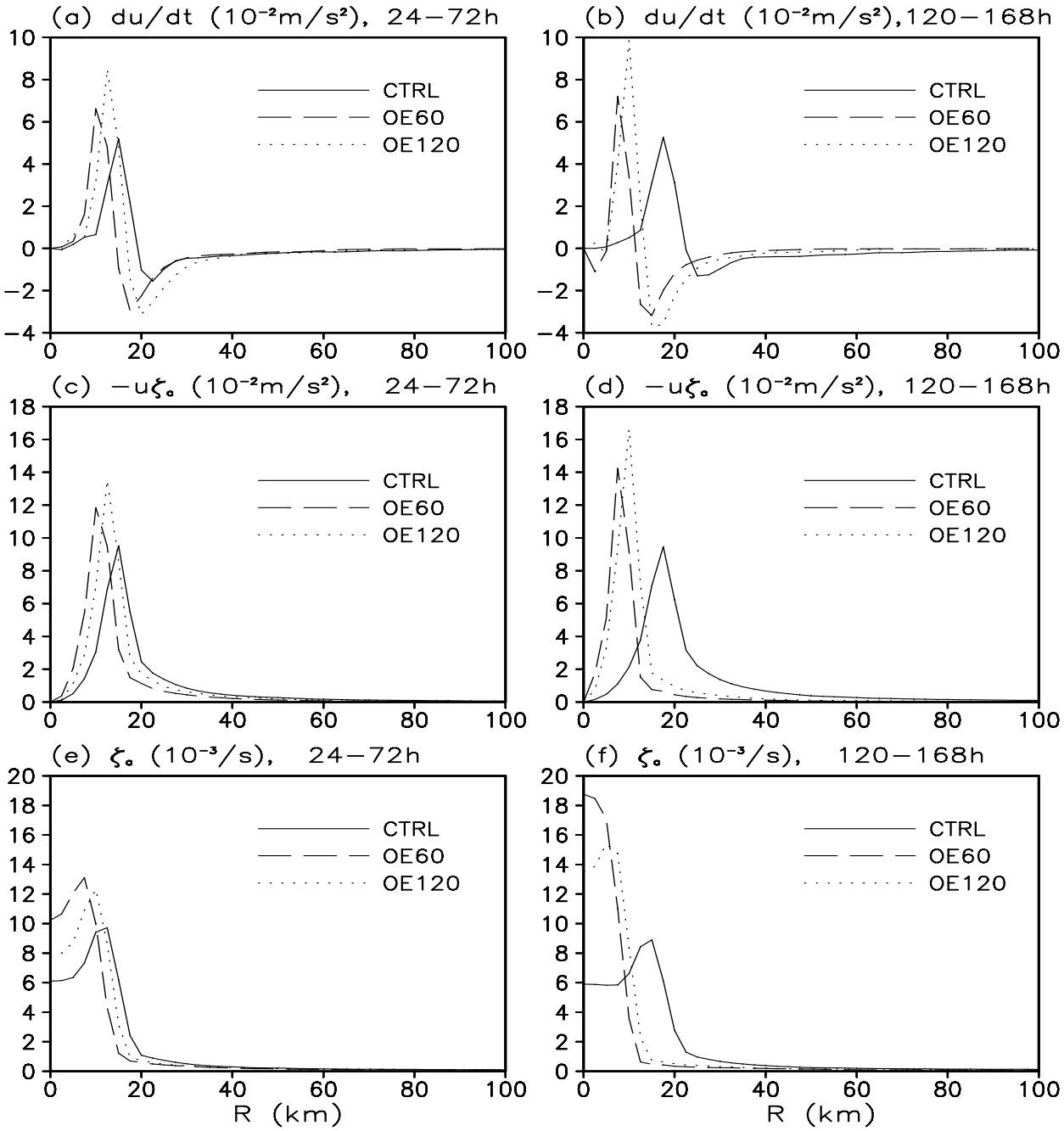

Figure 14. Azimuthal mean acceleration of radial wind (10^{-2} m s^{-2}, a and b), tendency of azimuthal mean tangential wind due to radial advection of absolute angular momentum ($-\overline{u}\overline{\varsigma}_a$, 10^{-2} m s^{-2}, c and d), and the azimuthal mean absolute vorticity (10^{-3} s^{-1}, e and f) at the lowest model level averaged between 24 and 72 h (a, c, and e) and between 120 and 168 h (b, d, and f) of integrations in experiments CTRL, OE60, and OE120.

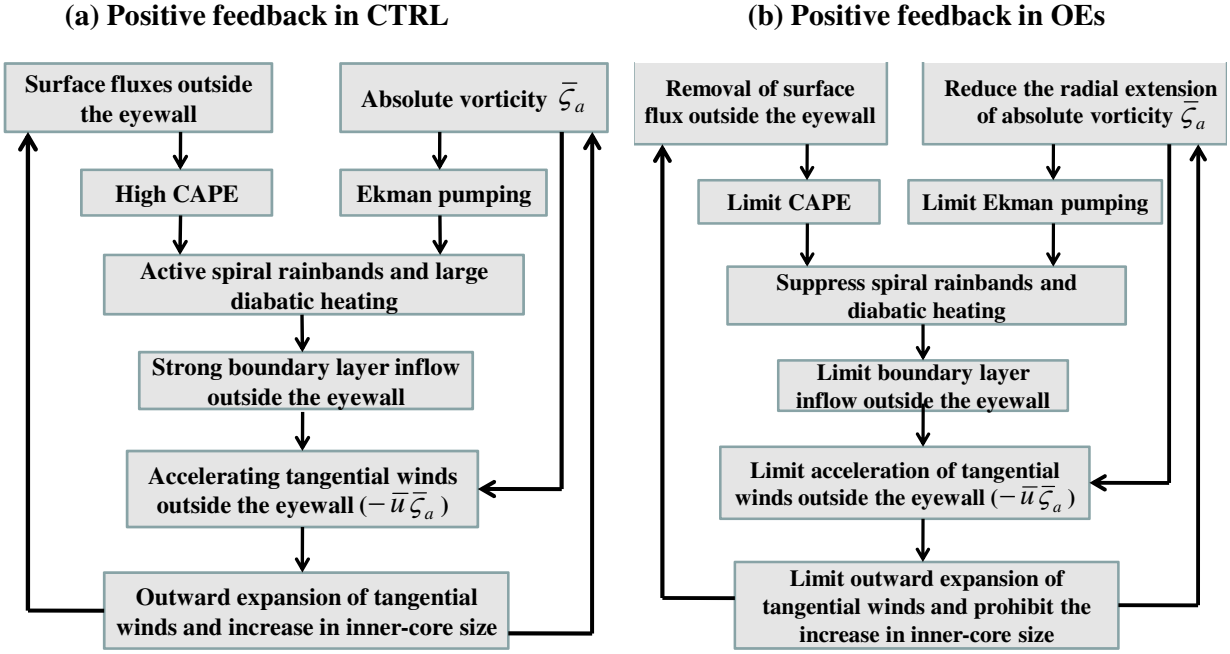

Figure 15. Schematic diagram showing the positive feedbacks that are responsible for the increase in the inner-core size of the simulated TC in the control experiment (a) and the decrease in the inner-core size for the simulated TCs in all OEs (b). See text for details.